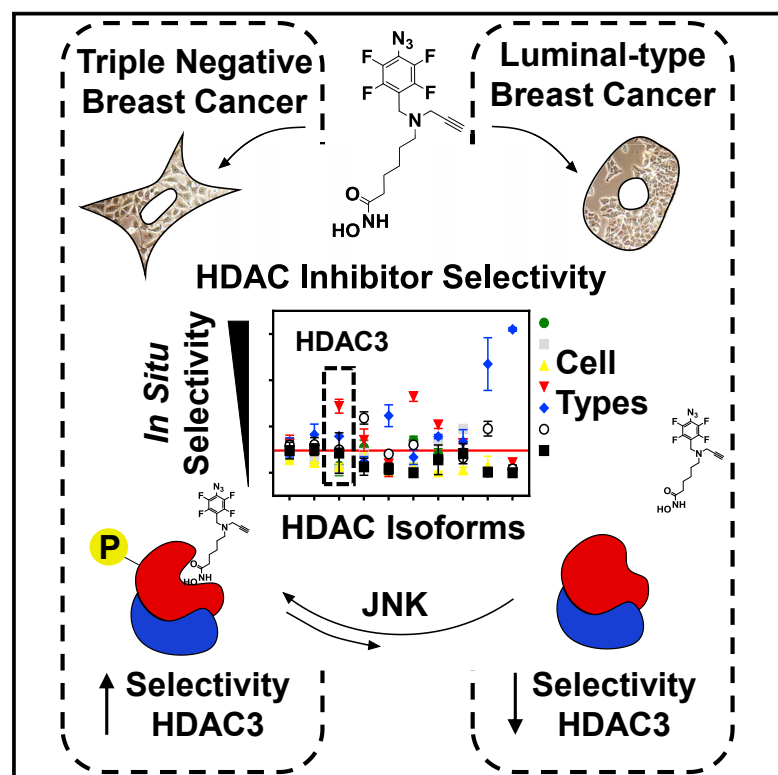


Cell Chemical Biology

Divergent JNK Phosphorylation of HDAC3 in Triple-Negative Breast Cancer Cells Determines HDAC Inhibitor Binding and Selectivity

Graphical Abstract



Authors

Thomas W. Hanigan,
Shaimaa M. Aboukhatwa,
Taha Y. Taha, Jonna Frasier,
Pavel A. Petukhov

Correspondence

pap4@uic.edu

In Brief

Hanigan et al. developed a method to identify relevant HDAC isoforms associated with inhibitor efficacy in breast cancer cells. They found c-Jun N-terminal kinase phosphorylation increases inhibitor binding and selectivity, and causes divergent regulation of HDAC3 in triple-negative versus luminal cells.

Highlights

- Comprehensive analysis of HDAC inhibitor selectivity reveals cell type dependence
- HDAC3 activity is divergently regulated by phosphorylation in triple-negative cells
- c-Jun N-terminal kinase phosphorylates HDAC3
- HDAC3 phosphorylation increases binding and alters selectivity of HDAC inhibitor



Divergent JNK Phosphorylation of HDAC3 in Triple-Negative Breast Cancer Cells Determines HDAC Inhibitor Binding and Selectivity

Thomas W. Hanigan,¹ Shaimaa M. Aboukhatwa,^{1,2} Taha Y. Taha,¹ Jonna Frasor,³ and Pavel A. Petukhov^{1,4,*}

¹Department of Medicinal Chemistry and Pharmacognosy, College of Pharmacy, University of Illinois at Chicago, 833 South Wood Street, Chicago, IL 60612, USA

²Department of Pharmaceutical Chemistry, Faculty of Pharmacy, Tanta University, Tanta, Egypt 31527

³Department of Physiology and Biophysics, University of Illinois at Chicago, Chicago, IL 60612, USA

⁴Lead Contact

*Correspondence: pap4@uic.edu

<http://dx.doi.org/10.1016/j.chembiol.2017.08.015>

SUMMARY

Histone deacetylase (HDAC) catalytic activity is regulated by formation of co-regulator complexes and post-translational modification. Whether these mechanisms are transformed in cancer and how this affects the binding and selectivity of HDAC inhibitors (HDACis) is unclear. In this study, we developed a method that identified a 3- to 16-fold increase in HDACi selectivity for HDAC3 in triple-negative breast cancer (TNBC) cells in comparison with luminal subtypes that was not predicted by current practice measurements with recombinant proteins. We found this increase was caused by c-Jun N-terminal kinase (JNK) phosphorylation of HDAC3, was independent of HDAC3 complex composition or subcellular localization, and was associated with a 5-fold increase in HDAC3 enzymatic activity. This study points to HDAC3 and the JNK axes as targets in TNBC, highlights how HDAC phosphorylation affects HDACi binding and selectivity, and outlines a method to identify changes in individual HDAC isoforms catalytic activity, applicable to any disease state.

INTRODUCTION

Aberrant changes in the epigenetic landscape of chromatin is a hallmark of cancer (ENCODE Project Consortium, 2012). These changes are a function of the enzymes that catalyze the reading, writing, and erasing of the post-translational modifications (PTMs) on DNA and associated histones. Histone deacetylase (HDAC) is a family of enzymes responsible for catalyzing the removal of acetyl marks from histone proteins and, as such, have been implicated in a number of different cancers, including breast cancer (Glozak and Seto, 2007). While HDAC inhibitors (HDACis) have shown promise as breast cancer therapeutics (Munster et al., 2009; Luu et al., 2008), HDACs are intimately involved in normal cellular signaling and some of the 18 human isoforms or classes of these isoforms have been shown to be

involved with tumor suppression (Taylor et al., 2011; Ropero et al., 2006; Bhaskara et al., 2010; Heideman et al., 2013; Pulkuri et al., 2007). Given the pleiotropic nature of HDACs in cancer, the current paradigm is to selectively inhibit one or more of the 18 human isoforms associated with tumor initiation and progression (Ontoria et al., 2009; Khan et al., 2008; Fournel et al., 2008; Balasubramanian et al., 2008). However, it remains unclear which isoforms are important to target for efficacy in breast cancer. Correlational studies between individual isoform expression and disease state in breast cancer have been disparate (Lapierre et al., 2016; Zhang et al., 2005b; Muller et al., 2013; Hsieh et al., 2016). In addition to expression, HDAC activity can be regulated through formation of multi-protein complexes and PTMs (Zhang et al., 1999, 2005a; Guenther et al., 2000; Pflum et al., 2001). Whether these mechanisms are transformed in breast cancer, or any other disease state, remains unclear owing to a lack of methodology to easily identify changes in HDAC catalytic activity. If these changes are occurring, it will also be important to ascertain how this regulation affects HDACi binding in cells, subsequently termed target engagement.

Considering that photoreactive probes have already proven to be invaluable tools to label HDACs in live cells (Salisbury and Cravatt, 2007; Xu et al., 2009), we designed photomate, a novel photoreactive hydroxamic acid-based HDACi probe. We compared the inhibition and binding of photomate to recombinant HDACs with engagement of HDACs in a panel of diverse breast cancer cell lines. We found that a subset of HDAC isoforms was differentially engaged in a cell type-dependent fashion, which was not predicted by assays with recombinant HDACs. Of particular interest, increased engagement of the class I HDAC3 was observed exclusively in triple-negative breast cancer (TNBC) cell lines. Following up on this observation, we systematically investigated the mechanisms contributing to photomate's divergent engagement of HDAC3 and found that its phosphorylation, through c-Jun N-terminal kinase (JNK), regulated HDACi target engagement. Ultimately, these differences reflected a change in the isoforms catalytic activity. Taken together we show a mechanism by which aggressive TNBC cells regulate the catalytic activity of an individual HDAC isoform. Given the efficacy of HDACis in these cell types, this isoform may serve as a pertinent drug target. In addition, we clearly show that regulation of this isoform affects inhibitor engagement

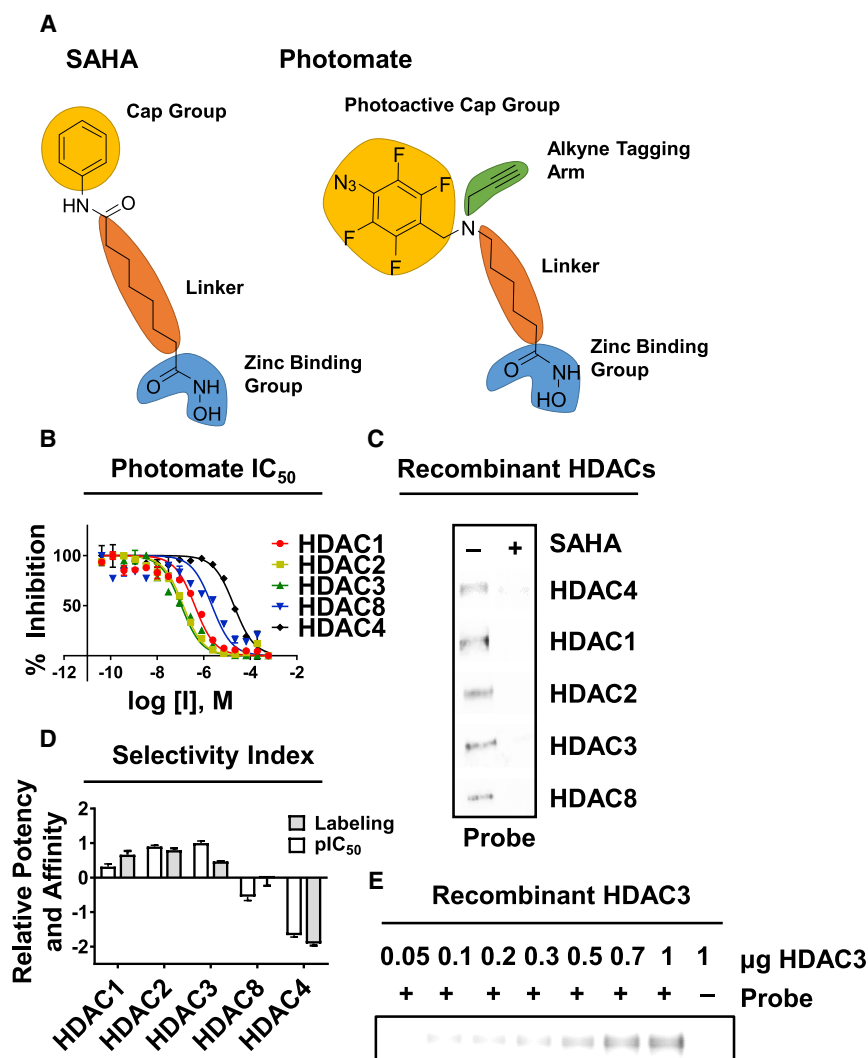


Figure 1. Photomate Inhibits and Labels Class I and II Recombinant HDACs

(A) Comparison of the archetypal pan HDAC inhibitor SAHA (Left) and photomate (right).

(B) IC_{50} measurements using recombinant class I or class II HDACs and fluorogenic substrates.

(C) Gel-based visualization of recombinant proteins labeled with photomate (lane 1) or photomate and SAHA (lane 2), followed by click reaction with azide-conjugated IRDye (gel is in grayscale).

(D) Relative potency or affinity as measured by pIC_{50} or labeling density. pIC_{50} or labeling density values were standardized to their mean and deviation and plotted. Data are shown as mean \pm SD. (E) Gel-based visualization as in (C) with standard dilutions of recombinant HDAC3. All results are representative of at least three independent experiments.

form covalent adducts with proximal proteins upon UV irradiation of the TFPA moiety. The alkyne arm facilitates the coupling of probe-protein adducts bio-orthogonally via copper-catalyzed 1,3-cycloaddition to an azide-conjugated fluorescent tag for visualization or biotin tag for enrichment and analysis.

Photomate Inhibits and Labels Class I and II HDACs

Using a traditional assay of isoform selectivity, we first verified that photomate was an inhibitor of recombinant class I and II HDACs using a fluorogenic assay. We found that photomate potently inhibits all class I HDACs with a half maximal inhibitory concentration (IC_{50}) ranging from 0.109 μ M (HDAC3) to 2.27 μ M

and selectivity in cells, which should be useful to increase accuracy in predicting HDACi selectivity *in vivo*. Furthermore, the pathway responsible for this type of regulation could be used to attenuate the effect of HDACis given this pathway controls HDACi engagement.

RESULTS

Design and Synthesis of a Photoreactive Hydroxamate-Based Probe, Photomate

In general, hydroxamic acid-based HDACis, such as the archetypal inhibitor suberoyl anilide hydroxamic acid (SAHA) consist of three components: (1) a zinc binding group, e.g., hydroxamic acid, to chelate the catalytic zinc in the active site of HDAC; (2) a surface binding “cap” group to interact with the rim of the active site of HDAC; and (3) a “linker” to connect the hydroxamic acid to the “cap” group (Figure 1A). Photomate incorporates a tetrafluorophenyl azide (TFPA) photoactivatable moiety, and an alkyne arm as the “cap” group, joined at a tertiary amine and connected via a five-carbon “linker” to a hydroxamic acid. This trifunctional design allows photomate to bind to the active site of HDACs and

(HDAC8), and inhibited HDAC4, a representative class II HDAC with an IC_{50} of 20.11 μ M (Figure 1B). Next, we explored photomate binding to recombinant HDACs by photolabeling individual isoforms with photomate, or with photomate and excess SAHA (Figure 1C). Photomate-protein adducts were reacted with an azide-conjugated 800CW IRDye for gel-based visualization. We observed effective labeling of all the recombinant class I and representative class II HDACs (Figure 1C). Labeling of all HDAC isoforms was lost upon co-incubation with SAHA (Figure 1C), indicating the labeling was active site dependent. In addition, we found that photomate could detect at least 0.1 μ g HDAC3 with this method (Figure 1E). Comparison of the relative potency or affinity based on inhibition or labeling respectively (Figure 1D) shows that photomate is non-selective for HDAC1, 2, and 3, but shows decreased potency and affinity with respect to HDAC8 and the class II HDAC4.

Photomate Differentially Targets HDACs Depending on Cell Type

To characterize the HDAC isoforms targeted by photomate in a cellular context where the mechanisms that regulate HDAC

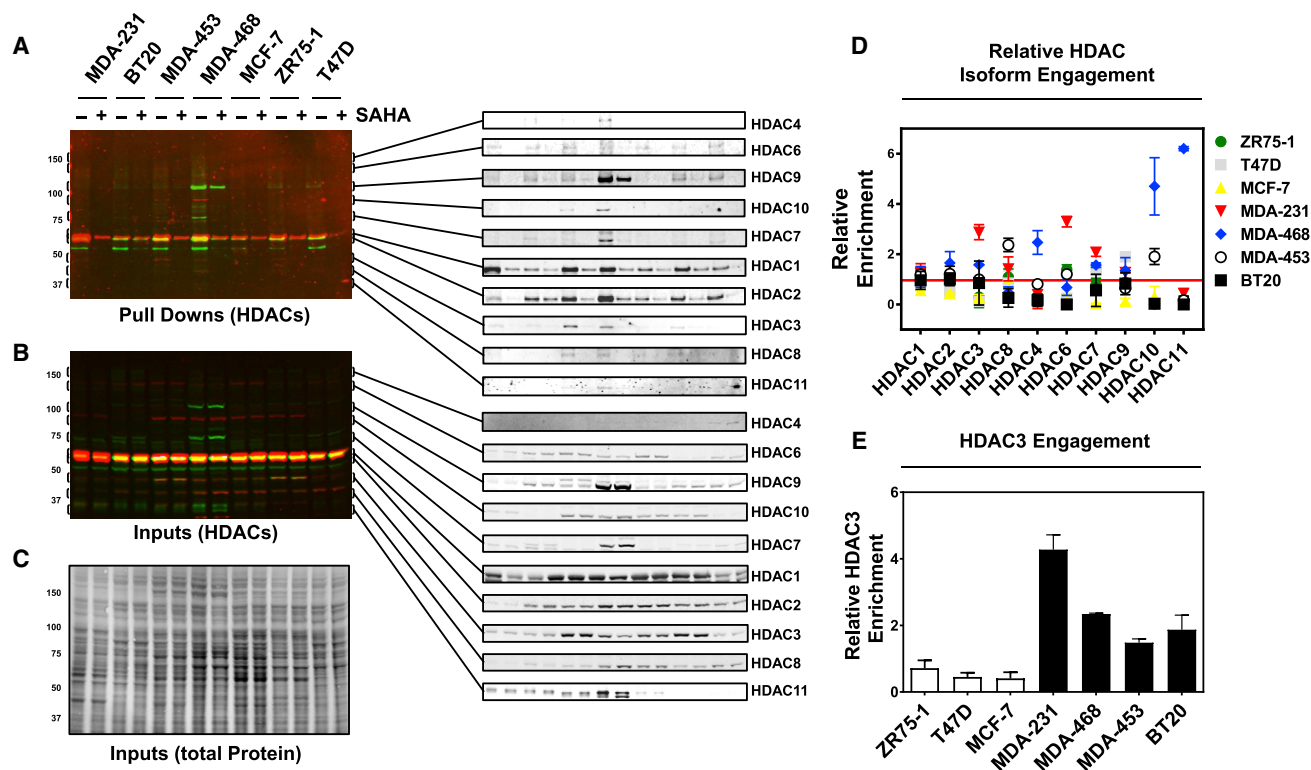


Figure 2. Photomate Differentially Targets HDACs Depending on Cell Type

(A) Western blot analysis of photomate-enriched fractions from seven breast cancer cell lines labeled *in situ* with photomate or photomate and excess SAHA. Samples were reacted with biotin azide tag, and enriched with streptavidin-coated magnetic beads. Antibodies for all class I and II HDACs were used for detection. Blot shows enriched fraction eluted off beads. Individual HDAC isoforms across all cell lines are blown up to the right and shown in grayscale for clarity. (B) Ten percent of input from each cell line used for enrichment experiments shown in (A); HDAC antibodies for all class I and II HDACs were used for detection. (C) Total protein staining of gel featured in (B).

(D) Quantification of enrichment experiments shown in (A, B, and C). Relative total abundance of each isoform across all cell types were normalized to total protein staining. Quantified enriched amounts of each isoform were then divided by the normalized total abundance of each isoform per cell line. These normalized values were then plotted with respect to the mean for each isoform across all cell types. All gels are representative of three individual experiments. Data are expressed as mean \pm SD.

(E) As in (D) but only for HDAC3 and without normalizing to the mean. Significantly different ($p < 0.0001$) values are separated by color (black and white). Data are expressed as mean \pm SD. For gel-based visualization of photomate targets, see Figure S2.

activity are intact, we conducted *in situ* photolabeling experiments in a panel of seven breast cancer cell lines (Figure 2). Altogether these cell lines represent the spectrum of breast cancer molecular subtypes, including luminal A (MCF-7, T47D), luminal B (ZR75-1), basal A (BT-20, MDA-MB-468), basal B (MDA-MB-231), and an additional cell line that does not fit into the classical breast cancer subtypes (MDA-MB-453). Cells growing in monoculture were incubated with photomate, photomate and excess SAHA, or vehicle control, followed by irradiation with 365 nm light. We reacted photomate-labeled samples with an azide-conjugated biotin tag for enrichment with streptavidin-coated beads and identification by western blot (Figure 2) and tandem mass spectrometry (MS/MS) analysis (MCF-7 cells only; Table S1; Figure 3C) or with an 800CW IRDye azide tag for gel-based visualization (Figure S2). Proteins enriched in photomate-labeled samples were compared with samples co-treated with excess SAHA, as well as samples treated with vehicle control, and were considered specific if the fluorescence density or spectral count was decreased by greater than 50% in

samples co-treated with photomate and excess SAHA and were not identified in vehicle controls. To account for variation in protein expression, we quantified the relative abundance of each class I and II HDAC in the cell lines (Figure 2B) and normalized the amount of each isoform that was specifically enriched to its relative abundance. These normalized values were then plotted with respect to the mean for each isoform across all cell types (Figures 2D and 2E).

In general, we found photomate ubiquitously targeted and enriched HDAC1, 2, and 9 from every cell line (Figures 2A and 2D). For these isoforms, the amounts enriched from each cell line correlated well with their relative expression in that cell line. This is reflected in the small range and SD of the relative enriched amounts of these HDAC isoforms across all cell lines, as shown in Figure 2D. However, all other class I and II HDACs were enriched only in a subset of cell types. For HDAC4 and 7, this was a result of only a subset of cell lines expressing this isoform (T47D, MDA-MB-468). On the other hand, the amounts of HDACs 3, 6, 8, 10, and 11 enriched by photomate did not

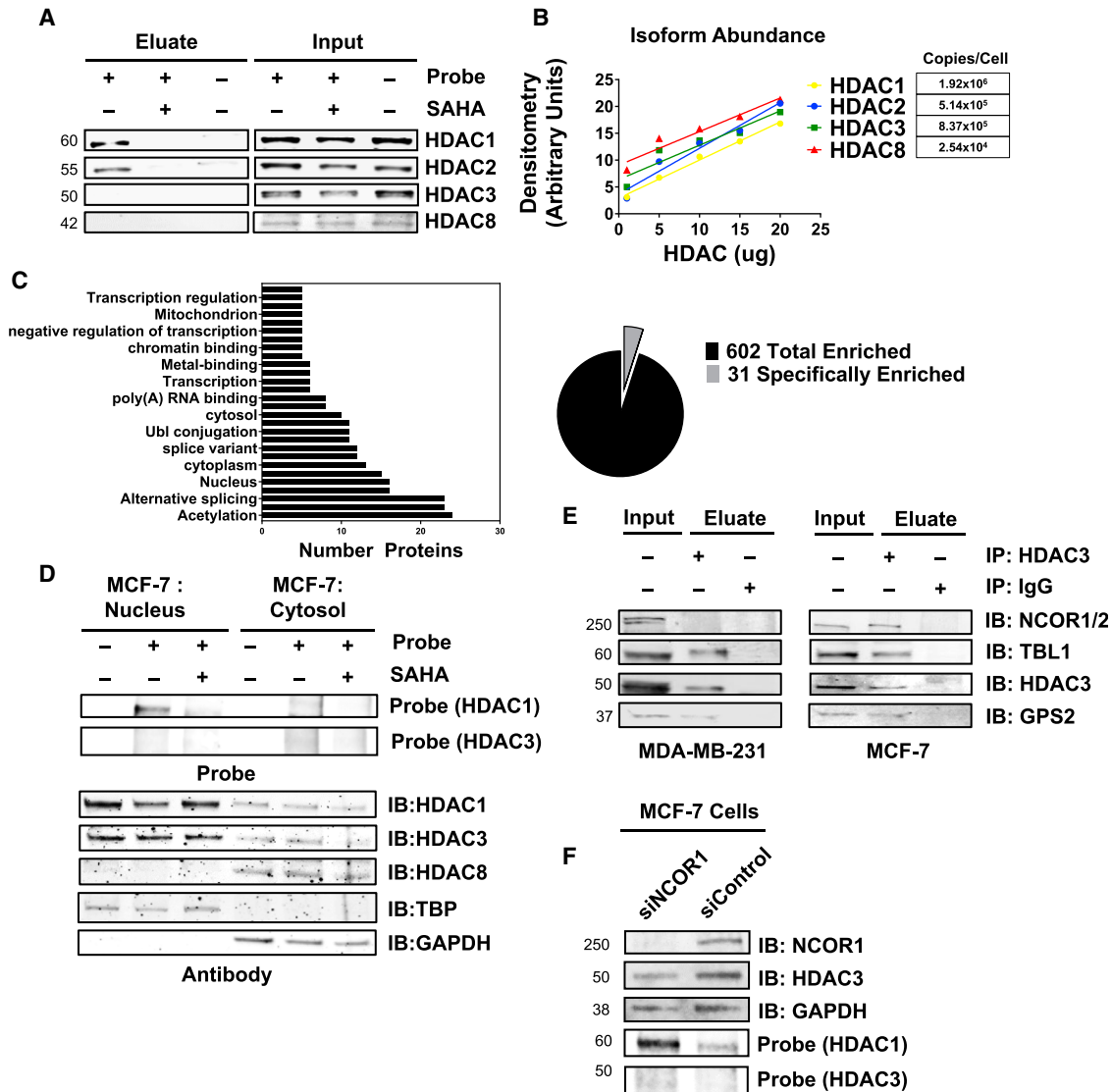


Figure 3. Divergent Engagement of HDAC3 Is Independent of Compartmentalization or Protein Complex Composition

(A) Western blot analysis of MCF-7 cells labeled *in situ* with photomate (lanes 1 and 4), photomate and SAHA (lanes 2 and 5), or DMSO (lanes 3 and 6), reacted with biotin azide tag, and enriched with streptavidin-coated magnetic beads. Blot shows enriched fraction eluted off beads and 2.5% of input recognized by anti-HDAC1, 2, 3, and 8 antibodies.

(B) Graph of the abundance of each class I HDAC in MCF-7 cells quantified by comparison of MCF-7 lysate with a standard curve of each recombinant class I HDACs; visualized by western blot (Figure S1).

(C) MS/MS analysis of photomate-enriched fractions, as in (A). Pie chart on the right shows total number of proteins identified by MS/MS and the number that were specifically enriched when compared with a DMSO control and were decreased by at least 50% when co-treated with SAHA. On the left, bioinformatic annotation of enriched proteins. All specifically enriched proteins are shown in Table S1.

(D) Gel-based visualization of MCF-7 cells labeled with photomate *in situ* followed by fractionation into cytosol (right) and nucleus (left). Probe staining is shown above, and antibody recognition of the same gel is shown below. Gels are in grayscale for clarity.

(E) Western blot analysis of HDAC3 co-immunoprecipitates. MDA-MB-231 cells, or MCF-7 cells were lysed and enriched with polyclonal anti-HDAC3 (Abcam) or rabbit IgG protein A bead conjugates (lanes 2 and 3, respectively). Eluates were analyzed by western blot along with 10% of input (lane 1) and blotted with antibodies for complex components.

(F) siRNA knock down of NCOR1 in MCF-7 cells. MCF-7 cells were transfected with siNCOR1 or siControl, followed by labeling with photomate and electrophoretic separation. Antibody recognition of transfected cells is shown above, followed by gel-based visualization of photomate engagement of HDAC1 and HDAC3 below. All results are representative of at least three independent experiments.

correlate with their relative expression. For example, we found significantly ($p < 0.0001$) increased amounts of HDAC3 were enriched from TNBC cell lines (black bars, Figure 2E) in comparison with luminal subtypes, such as MCF-7 (white bars, Figure 2E), despite increased expression in many of the luminal subtypes (Figure 2B). To illustrate this point we quantified the absolute abundance of each class I HDAC in MCF-7 cells, a cell line where we found little to no HDAC3 enrichment by western blot (Figures 3B and S1). HDAC1, 2, and 3 expression was very similar, with 1.92×10^6 , 5.14×10^5 , and 8.37×10^5 copies/cell, respectively. Notably, HDAC2 abundance is 1.6-fold lower than that of HDAC3, yet was enriched by photomate in this cell line while HDAC3 was not (Figures 3A and 3B). This finding is of particular interest given the trend differentiating TNBC and luminal subtypes, but also because it contradicts our *in vitro* experiments showing that photomate should be equipotent for HDAC1, 2, and 3. In addition, we comprehensively analyzed photomate targets in MCF-7 cells by MS/MS (Figure 3C, Table S1). This experiment matched western blot analysis in that HDAC1 and 2 were the only HDAC targets in this cell line, and also helped characterize several other non-HDAC zinc-containing enzymes or HDAC complex partners.

Divergent Engagement of HDAC3 Is Independent of Compartmentalization or Protein Complex Composition

Given the variation in HDAC3 and other class I and II HDAC engagement, we sought to gain insight into the mechanisms contributing to this variation. We investigated HDAC3 because its inhibition is generally thought to contribute to the efficacy of all FDA approved HDACis (Mottamal et al., 2015), and the mechanisms regulating its activity have been extensively explored. As HDAC3 translocates between nucleus and cytosol, we verified if photomate and HDAC3 have overlapping subcellular distribution. To do this we labeled MCF-7 cells, a cell line where photomate did not enrich HDAC3, followed by biochemical fractionation into cytosolic and nuclear portions (Figure 3D). Prominent labeling of HDAC1 and 2 was observed in the nucleus, showing that photomate can permeate the nuclear membrane. Antibody staining of the nuclear fraction showed that the majority of HDAC3 was in the nucleus as well; however, no labeling event was observed (Figure 3D).

In addition to subcellular localization, HDAC3 activity is regulated by formation of multi-protein complexes. Given that this has been shown to affect HDACi selectivity, we analyzed the stable components of the HDAC3 complex from cell lines that do (MDA-MB-231) or do not (MCF-7) show distinct photomate engagement of HDAC3 by co-immunoprecipitation. Figure 3E shows western blots of the immunoprecipitates enriched by a polyclonal HDAC3 antibody (Abcam). Known stable protein partners, TBL1, GPS2, and NCOR1, were co-immunoprecipitated with HDAC3 from MCF-7 cells; however, we noticed that NCOR1 was not enriched from MDA-MB-231 cells, the cell line with robust labeling of HDAC3. As NCOR1 and 2 are capable of directly activating HDAC3 enzymatic activity, we envisioned that this might also be capable of influencing photomate engagement of HDAC3. However, small interfering RNA (siRNA) knock down of NCOR1 in MCF-7 cells did not result in an increase in HDAC3 labeling (Figure 3F). Together these findings suggest that NCOR1 and potentially the protein complex composition

are, in general, not the underlying cause of the lack of HDAC3 labeling.

HDAC3 Engagement Is Correlated with Its Phosphorylation Status

In addition to transcriptional control of expression, subcellular localization, and co-repressor complex formation, HDAC3 is regulated by PTM. Phosphorylation of serine 424 occurs on the C terminus of HDAC3 and increases its activity (Zhang et al., 2005a). To investigate differences in HDAC3 phosphorylation, we utilized a phospho (Ser-424) HDAC3-specific antibody. We first validated the phospho HDAC3 (pHDAC3) antibodies specificity by phosphorylating recombinant HDAC3 using casein kinase II (CK2) (Zhang et al., 2005a). Figure S4A shows that HDAC3, incubated with CK2 in the presence of ATP, is recognized more by the pHDAC3 antibody, over HDAC3 incubated with CK2 only. In addition, we found that the polyclonal HDAC3 antibody from Abcam, used previously in this paper, equally recognized both the phosphorylated and non-phosphorylated forms of HDAC3, and that an antibody from Millipore recognized only the non-phosphorylated HDAC3 (Figure S4A).

Using these antibodies, we surveyed the phosphorylation state of HDAC3 in the panel of cell lines and found that significant ($p < 0.0001$) differences in the amounts of phosphorylated HDAC3 existed across cell types (Figure S3). Comparison of photomate's HDAC3 engagement and total pHDAC3 abundance shows a very high correlation ($R^2 = 0.822$), suggesting a linear relationship between photomate engagement of HDAC3 and its phosphorylation state (Figure 4A). Comparison of photomate's engagement of HDAC3 in comparison with HDAC1, normalized to their respective abundance (Figure 4B), shows that selectivity for HDAC3 is significantly increased in those cell lines with highly phosphorylated HDAC3 ($p < 0.0001$) and in comparison with *in vitro* experiments with recombinant HDACs.

HDAC3 Engagement Is Directly Affected by Its Phosphorylation

To test whether HDAC3 phosphorylation was capable of directly affecting photomate binding, we evaluated photomate's ability to label recombinant phosphorylated HDAC3 in comparison with recombinant HDAC3. What we observed was a more than 4-fold increase in photomate labeling of phosphorylated HDAC3 (Figure 4C). This experiment shows that HDAC3 phosphorylation alone is capable of causing an increase in photomate binding to HDAC3. We verified that this was also the case in cells by transfecting plasmids for either a S424A, S405A, or control FLAG-tagged HDAC3 into MDA-MB-231 cells followed by photomate labeling and enrichment with FLAG antibodies. In agreement with the binding experiments using recombinant phosphorylated HDAC3, we found the S424A mutant had decreased photomate labeling in comparison with the S405A and control FLAG HDAC3, both of which became phosphorylated after expression (Figure 4D). This conclusion seems rational, as others have proposed that HDAC3 activity increases in cells upon phosphorylation (Zhang et al., 2005a). A change in HDAC3 enzymatic activity is likely due to changes in its tertiary structure, which would also interfere with photomate binding. To verify that the enzymatic activity of HDAC3 is indeed increased when phosphorylated, we compared phosphorylated HDAC3's

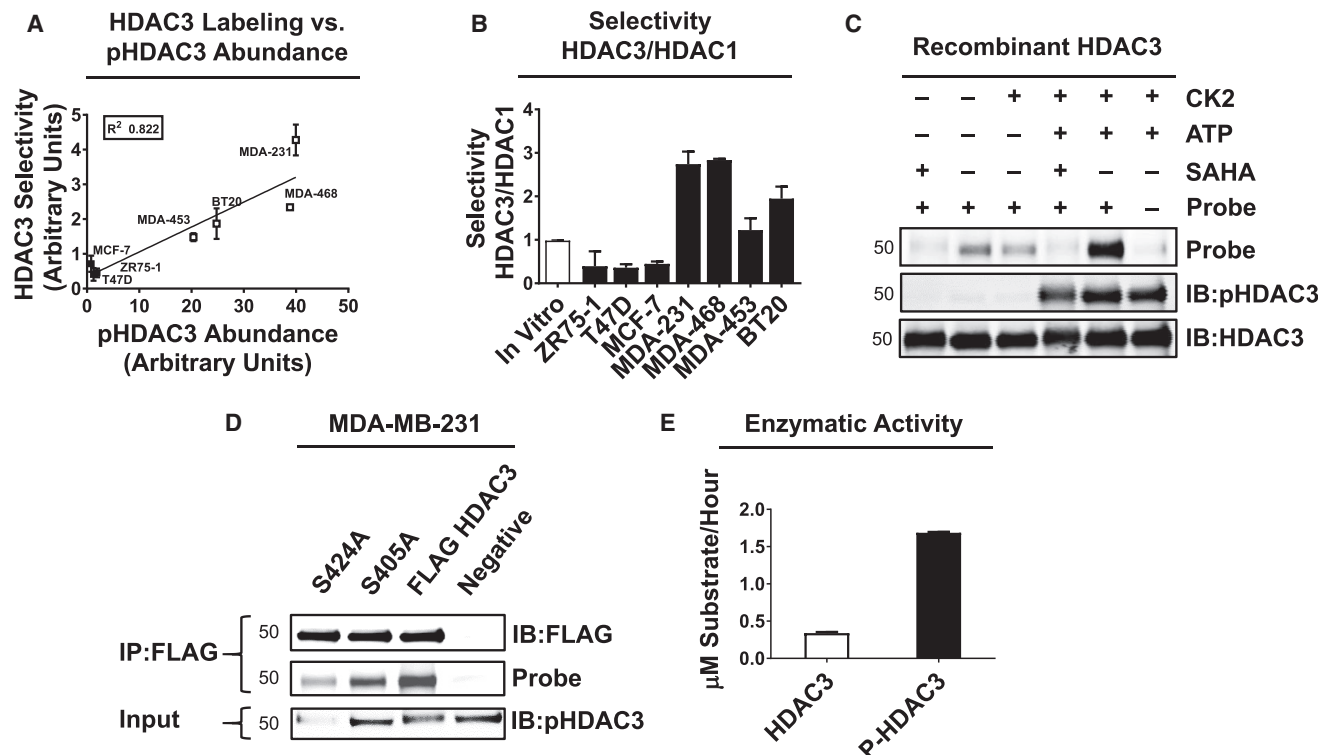


Figure 4. HDAC3 Phosphorylation Directly Increases Inhibitor Binding

(A) Comparison of HDAC3 engagement versus relative abundance of phosphorylated HDAC3 (pHDAC3) protein; as quantified by western blot (Figure S3). Linear regression and R^2 values are shown.

(B) Statistically significant differences in photomate selectivity for HDAC3 compared with HDAC1 across cell lines and in comparison with selectivity based on *in vitro* potency. One-way ANOVA shows $p < 0.0001$. Data are shown as mean \pm SD.

(C) Gel-based visualization of recombinant HDAC3 incubated with CK2 and ATP or with CK2 and vehicle followed by labeling with photomate. Probe labeling is shown at the top followed by staining with antibody below.

(D) Differential labeling of FLAG-tagged HDAC3 mutants. MDA-MB-231 cells were transfected with mutant or control HDAC3 plasmids, labeled with photomate (all lanes), and enriched with FLAG antibodies. Visualization of probe or antibody signals of the immunoprecipitates are shown above, and input staining of the phosphorylated HDAC3 below.

(E) Enzymatic activity of HDAC3 and pHDAC3 was analyzed using a synthetic class I HDAC substrate. Activity is expressed in μM substrate/hour. Student's *t* test shows $p < 0.0001$. Data are expressed as mean \pm SD. All results are representative of at least three independent experiments.

ability to deacetylate a synthetic fluorogenic substrate to that of recombinant HDAC3. As seen in Figure 4E, the activity of phosphorylated HDAC3 is, on average, five times greater than that of the non-phosphorylated HDAC3. Taken together, these experiments suggest that phosphorylation of HDAC3 at serine 424 directly affects both photomate binding and HDAC3 activity *in vitro* and in cells.

JNK Controls HDAC3 Phosphorylation and Photomate Engagement of HDAC3

After establishing that phosphorylation of HDAC3 governs inhibitor binding, we sought to understand the cause of the differential HDAC3 phosphorylation between cell lines. Because CK2 readily phosphorylates recombinant HDAC3, we hypothesized that differential CK2 activity leads to the variation in HDAC3 phosphorylation. To test this hypothesis, we treated MDA-MB-231 cells with two structurally diverse kinase inhibitors that have been shown to potently inhibit CK2 activity (TBB and LY294002) (Gray et al., 2014; Gharbi et al., 2007), followed by labeling with photomate. Neither of the compounds induced

any change in HDAC3 engagement or phosphorylation state, despite significantly changing phosphorylation of CK2 substrates AKT or c-Jun (Figures S4B, 6H, and 6I). In addition to CK2, it has been shown that GSK3b can phosphorylate HDAC3 in neurons (Bardai and D'Mello, 2011). However, addition of the GSK3b inhibitor AR-A014418 did not affect HDAC3 phosphorylation or photomate engagement (Figure S5D). This is in line with the experiment using LY294002, as it has been shown to increase GSK3b activity through AKT in MDA-MB-231 cells (Li et al., 2014). Taken together these experiments suggest that the activity of CK2 or GSK3b does not affect HDAC3 phosphorylation in MDA-MB-231 cells.

Given the TNBC cell lines show HDAC3 labeling, but estrogen receptor (ER)-positive luminal cell lines do not, we initially thought that ER may play a role in decreasing HDAC3 phosphorylation and photomate engagement. We tested this hypothesis by incubating MCF-7 cells with tamoxifen, at a concentration shown to antagonize ER activity in MCF-7 cells (Frasor et al., 2006), or with siRNA specific for ER α , followed by labeling with photomate (Figures S4C and S4D). We found no increase in

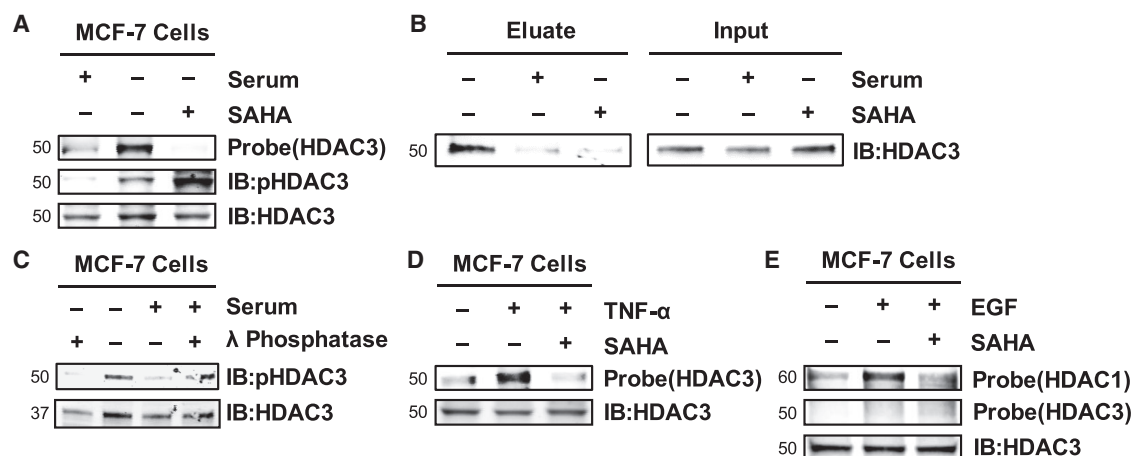


Figure 5. HDAC3 Phosphorylation and Photomate Engagement Is Affected by Cellular Stress

(A) Gel-based visualization of MCF-7 cells either serum starved or grown in medium supplemented with 10% fetal bovine serum (FBS) and labeled *in situ* with photomate or photomate and SAHA. Recognition of photomate-labeled HDAC3 with antibodies is shown below.

(B) Western blot analysis of MCF-7 cells, serum starved, labeled with photomate or photomate and SAHA *in situ*, reacted with biotin azide tag, and enriched with streptavidin-coated magnetic beads. Blot shows enriched fraction eluted off the beads and 2.5% of input stained with HDAC3 antibodies.

(C) Western blot analysis of pHDAC3 in MCF-7 cells either serum starved or grown in medium supplemented with 10% FBS. Each group was incubated with lambda phosphatase to remove any phosphate groups from HDAC3.

(D) Gel-based visualization of MCF-7 cells either treated with TNF- α or vehicle and labeled *in situ* with photomate or photomate and SAHA. Recognition of the photomate-labeled HDAC3 with antibodies is shown below.

(E) As in (D) with EGF treatment in place of TNF- α . All results are representative of at least three independent experiments (for additional experiments and controls, see Figures S4 and S5).

HDAC3 labeling or HDAC3 phosphorylation as a result of either of these experiments, indicating that ER expression or activity does not affect photomate engagement of HDAC3.

While TNBC cell lines do not rely on ER signaling to proliferate, many have constitutive activation of MAPK signaling, through increased expression of epidermal growth factor receptor (EGFR) or Ras mutation (Cossu-Rocca et al., 2015). As the NCOR-HDAC3 complex has been shown to be regulated by MAPK signaling (Jonas and Privalsky, 2004), we hypothesized that this signaling pathway may increase photomate engagement of HDAC3. To test this hypothesis, we tried either removal or addition of known MAPK-stimulating agents, followed by labeling with photomate in MCF-7 cells. In opposition to our hypothesis, we found that serum starvation, as well as treatment with the proinflammatory cytokine tumor necrosis factor alpha (TNF- α), induces specific labeling of HDAC3 in MCF-7 cells (Figures 5A–5D, S5A, and S5I), whereas the addition of MAPK-stimulating growth factors, EGF and IGF-1, had no effect despite inducing changes in phosphorylation of AKT (Figures 5E, S5B, and S5J). In line with our experiments from Figure 4, showing that photomate engagement of HDAC3 is associated with HDAC3 phosphorylation, the increase in HDAC3 labeling induced by serum starvation corresponded with a concomitant increase in HDAC3 phosphorylation, which was labile to λ -phosphatase (Figures 5A and 5C). In addition, we observed that most MCF-7 cells were aligned in G₀/G₁ upon serum starvation prior to labeling with photomate (Figure S5C). Taken together, these experiments show that mitogen removal and inflammatory cytokine stimulation induce HDAC3 phosphorylation and photomate engagement of HDAC3, whereas addition of growth factors has no effect.

Because removal of serum or inflammatory cytokine signaling increased HDAC3 phosphorylation and photomate engagement, we hypothesized that a stress-activated protein kinase pathway, either nuclear factor κ B (NF- κ B), p38, or JNK was responsible. To test this hypothesis, we used inhibitors of IKK (IKK VII), p38 (SB202190), or JNK (SP600125) at concentrations that altered phosphorylation of known substrates of their respective enzymes (Figures 6H and 6I), followed by labeling with photomate. We found that the JNK inhibitor abolished the labeling of HDAC3 (Figures 6A, 6B, S5G, and S5H), whereas the IKK inhibitor had no change and the p38 inhibitor increased labeling (Figures S5E and S5F). Because the JNK inhibitor decreased labeling, we again measured the phosphorylation state of HDAC3 in comparison with control and observed a complete loss of HDAC3 phosphorylation (Figures 6A and 6B). In addition to SP600125, we used another structurally distinct specific JNK inhibitor (TCS JNK 60) in conjunction with photomate labeling and found both HDAC3 labeling and phosphorylation were decreased (Figure 6C). In agreement with JNK phosphorylating HDAC3, we identified activated JNK (phosphorylated) in MDA-MB-231 cell lysates immunoprecipitated with HDAC3 antibodies (Figure 6G). Furthermore, there were higher levels of phosphorylated JNK detected in the group of cell lines that were previously shown to have increased HDAC3 phosphorylation and photomate engagement (Figure 6F). Finally, we found recombinant JNK1 in the presence of ATP-phosphorylated recombinant HDAC3 (Figure 6E). These experiments demonstrate that increased JNK activity leads to an increase in HDAC3 phosphorylation and HDACi engagement of HDAC3 in the basal type cell lines. To test whether JNK activity also controls HDAC3 phosphorylation in luminal subtypes, we pretreated MCF-7 cells with JNK inhibitor (TCS JNK 60)

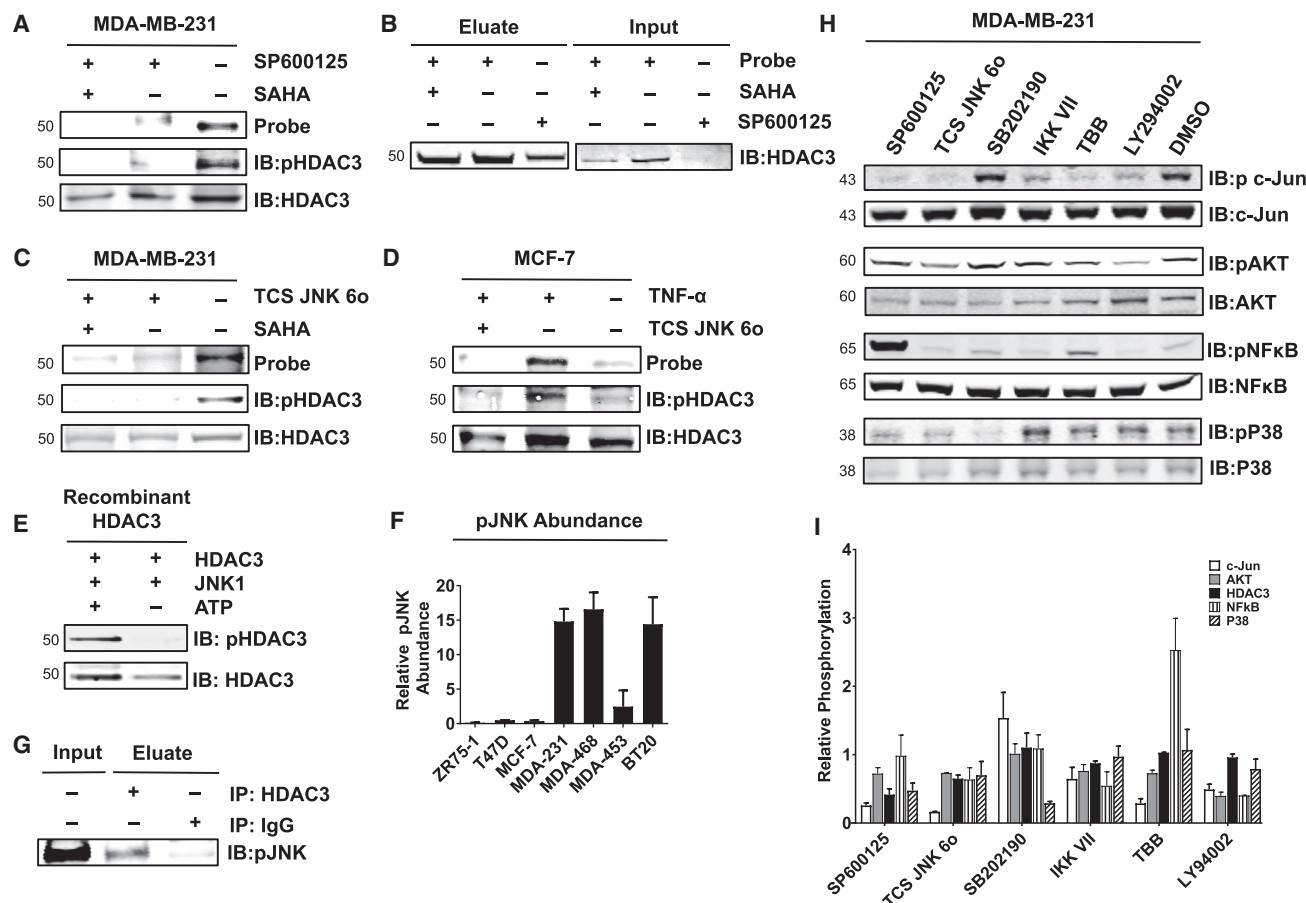


Figure 6. JNK Signaling Controls HDAC3 Phosphorylation

(A) Gel-based visualization of MDA-MB-231 cells either treated with SP600125 or vehicle and labeled *in situ* with photomate or photomate and excess SAHA. Recognition of photomate-labeled HDAC3 with antibodies is shown below.

(B) Western blot analysis of MCF-7 cells treated with SP600125, labeled with photomate or photomate and excess SAHA *in situ*, reacted with biotin azide tag, and enriched with streptavidin-coated magnetic beads. Blot shows enriched fraction eluted off the beads and 2.5% of input stained with HDAC3 antibodies.

(C) As in (A) substituting TCS JNK 6o for SP600125.

(D) Gel-based visualization of TNF- α -treated cells either pretreated with TCS JNK 6o or vehicle, and labeled *in situ* with photomate (all lanes). Recognition of photomate-labeled HDAC3 with antibodies is shown below.

(E) Western blot analysis of recombinant HDAC3 incubated with JNK in the presence or absence of ATP.

(F) Graph showing pJNK abundance in each cell line as quantified from western blot in Figure S3. Data are shown as mean \pm SD.

(G) pJNK is detected in HDAC3 co-immunoprecipitates or IgG control. Ten percent of input is shown in lane 1.

(H and I) Western blot analysis of changes in several kinase pathways induced by treatment of MDA-MB-231 cells with all inhibitors used in this study and (I) quantification of (H) normalized to treatment with vehicle. All results are representative of at least three independent experiments. Data are expressed as mean \pm SD.

and stimulated them with TNF- α . We observed a decrease in HDAC3 labeling and phosphorylation in comparison with cells treated with TNF- α alone, and similar levels to cells treated with neither TNF- α or JNK inhibitor (Figure 6D).

DISCUSSION

It has been shown that HDAC activity is aberrantly regulated in cancer by specific recruitment to genomic loci, and change in expression. In addition to these mechanisms, HDAC activity depends on formation of co-repressor complexes and PTMs; however, it is unclear whether these mechanisms are transformed in cancer due to a lack of methodology. In this study,

we provide the first evidence that HDAC phosphorylation is transformed in TNBC cell lines by analyzing the engagement of a novel photoreactive HDACi probe. This method not only helps to understand a mechanism by which a subset of breast cancer cell lines regulate HDAC activity, but has implications for the future design and current understanding of the way HDACis exert their effect.

Comparison of photomate's selectivity, based on inhibition of, or binding to, recombinant HDACs, versus its engagement of HDACs in cells, revealed significant differences with respect to HDAC3 that did not correlate with HDAC3 abundance. While photomate could bind to and inhibit HDAC3 under the conditions used for determination of IC₅₀, engagement in MCF-7 cells and

other luminal cell types could not be detected. In contrast to this, we found TNBC cells had increased engagement of, and selectivity for, HDAC3 in comparison with recombinant HDACs. Differential engagement across cell types was also observed for most other class I and II HDACs, suggesting that target engagement in cells can differ from *in vitro* predictions for these isoforms as well. As the development of selective HDACis is often guided by studies with recombinant HDACs, this variation clearly demonstrates that the actual target in a context of interest may be misrepresented by recombinant-based assays.

Investigation into the mechanisms regulating HDAC3 binding revealed that HDAC3 phosphorylation, but not subcellular distribution or protein complex composition, directly controls photomate engagement. We found that increased HDAC3 phosphorylation strongly correlated with engagement of HDAC3 in the cell lines under investigation. We validated that phosphorylation could directly control inhibitor binding, irrespective of other HDAC3 complex components, by comparing photomate binding to phosphorylated and non-phosphorylated recombinant HDAC3, which showed 4-fold higher photomate binding to phosphorylated HDAC3. We found that this was true in cells as well because photomate engagement of a S424A HDAC3 mutant was decreased in comparison with control phosphorylated HDAC3. Furthermore, changing HDAC3 phosphorylation through inhibition of an HDAC3 kinase also significantly affects HDAC3 engagement in cells. In addition to differences in phosphorylation, we found that all known stable HDAC3 complex components were equally accounted for apart from NCOR1. Elimination of this discontinuity, however, did not influence photomate binding in cells, but the tertiary structure of the remaining components, or binding of a transient or unknown component, could potentially affect photomate binding concurrently with HDAC3 phosphorylation. Based on this data, accounting for phosphorylation when conducting *in vitro* assays may lead to a more accurate assessment of selectivity in cells.

In addition to its effect on inhibitor binding, we found that phosphorylation of recombinant HDAC3 exhibits a 5-fold higher catalytic activity compared with the non-phosphorylated protein. Because TNBC cells have increased HDAC3 phosphorylation in comparison with luminal subtypes, and thus increased HDAC3 catalytic activity, they may be more reliant on its catalytic activity. As we have observed, photomate (Figure S2B), as well as other HDACis (Tate et al., 2012; Uehara et al., 2012), have increased efficacy in TNBC cells, HDAC3 may be a pertinent isoform to target for treatment of TNBC. However, cell type-based variation in other isoforms was observed, and likely contributes to the variation in efficacy as well. A follow-up study with a larger set of cell lines or patient-derived samples would be necessary to determine statistically significant correlations between targeted HDACs and efficacy.

Others have observed cell type-dependent effects of HDACis in transformed cells as well, which may be explained by the differences in HDACi selectivity observed in this study. For example, many cell-based and *in vivo* studies have shown different mechanisms of cell death in response to HDACis, including activation of intrinsic (Insinga et al., 2005; Singh et al., 2005) versus extrinsic (Chakraborty et al., 2013; Ruefli et al., 2001) apoptotic pathways, or cell-cycle arrest through induction of CDKN1A (Richon et al., 2000; Sandor et al., 2000),

leading to cell type-dependent efficacy. To account for these differences and determine where treatment with HDACis may be beneficial, diagnostic indicators of HDACi efficacy are needed. While several genomic approaches correlating HDACi response with mutational landscape or changes in basal gene expression serve as invaluable tools to identify prognostic markers associated with HDACi efficacy (Rees et al., 2016; Garnett et al., 2012), our study compliments this approach by identifying direct changes in HDAC binding, selectivity, and enzymatic activity, which may also affect HDACi efficacy.

Although we explored a number of different key pathways shown to involve HDAC3, including ER (Liu and Bagchi, 2004), CK2 (Zhang et al., 2005a), NF- κ B (Gao et al., 2005), p38 (Mahlknecht et al., 2004), and other MAPK-mediated signaling, we found that only the JNK pathway regulates HDAC3 phosphorylation. Others have observed a connection between JNK and HDAC3 as well (Weiss et al., 2003; Zhang et al., 2002); we add that increased JNK phosphorylation leads to HDAC3 phosphorylation, which affects both enzymatic activity and inhibitor binding in basal breast cancer cells in comparison with luminal subtypes. This is in line with other observations showing luminal breast cancer cells often have inactivating mutations to MAP3K1 and MAP2K7, the kinases directly upstream of JNK that are responsible for its phosphorylation and activation (Ellis et al., 2012). We envision that measuring HDAC3 phosphorylation and/or JNK pathway mutations such as MAP3K1 and MAP2K7 could serve as diagnostic markers for predicting cellular response to treatment with HDACis. Finally, preclinical data suggest that inhibition of MAPK signaling, specifically the EGFR, in conjunction with HDACis is more effective in a broad range of cancer types (Lai et al., 2010; Bruzzese et al., 2011), and clinical trials are ongoing. Our study provides a rationale for co-targeting the JNK pathway, a specific downstream component of an individual MAPK pathway, with HDAC3 to enhance the effects of HDACis in cancer therapy.

Beyond breast cancer, comparison of the differences in photomate binding to recombinant proteins against any disease state of interest should ultimately serve as a method to determine differences in catalytic activity of an individual HDAC isoform between these contexts; exposing novel drug targets and novel HDAC regulatory mechanisms.

SIGNIFICANCE

Abnormal histone modifications are a hallmark of cancer. Histone deacetylase is a family of enzymes comprised of 18 human isoforms that catalyze the removal of acetyl marks from histone tails. HDACs have been shown to be aberrantly recruited to specific genomic loci, and expression of individual isoforms is often altered in a number of cancer types. HDAC catalytic activity is also regulated post translationally by phosphorylation, subcellular localization, and protein complex formation. However, it is unclear whether these mechanisms are utilized in cancer, as no methods to detect these changes for individual isoforms exist. Given the interest in development of isoform-selective HDACis, it is also important to determine what affect this type of regulation has on HDACi target engagement. In this paper, we developed a novel method that enabled the discovery of divergent

regulation of HDAC3 through phosphorylation by c-Jun N-terminal kinase (JNK) in TNBC, and observed variable cellular selectivity that was not predicted by standard measurement with recombinant enzymes. Identification of this HDAC3 regulation and its effect on inhibitor binding will allow development of compounds targeting phosphorylated HDAC3 or combination therapies involving the JNK axis, improve prediction of HDACi selectivity *in vivo*, and outline a method for detecting changes in an individual HDAC isoforms catalytic activity in any disease state of interest.

STAR★METHODS

Detailed methods are provided in the online version of this paper and include the following:

- KEY RESOURCES TABLE
- CONTACT FOR REAGENT AND RESOURCE SHARING
- EXPERIMENTAL MODEL AND SUBJECT DETAILS
 - Cellular Models
- METHOD DETAILS
 - Fluorogenic Enzymatic Assays for Class I HDAC Isoforms
 - General Procedure for Photolabeling in Live Cells
 - Mass Spectrometry Analysis
 - Serum Starvation Followed by Photolabeling
 - Treatment with Inhibitors, Cytokines and Growth Factors Followed by Photolabeling
 - Transfection of Mutant HDAC3 Followed by Photolabeling
 - Western Blotting
 - Quantitation of Class I HDAC Isoforms in Breast Cancer Cell Lines
 - Photolabeling of Recombinant Proteins
 - Phosphorylation of Recombinant HDAC3
 - Enzymatic Activity of HDAC3
 - Immunoprecipitations
 - Compound Synthesis
- QUANTIFICATION AND STATISTICAL ANALYSIS
- DATA AND SOFTWARE AVAILABILITY

SUPPLEMENTAL INFORMATION

Supplemental Information includes five figures and one table and can be found with this article online at <http://dx.doi.org/10.1016/j.chembiol.2017.08.015>.

AUTHOR CONTRIBUTIONS

T.W.H. and P.A.P. conceived of the project. T.W.H. designed and performed all experiments and data analysis apart from determination of IC₅₀ and comparison of enzymatic activity, which was done by S.M.A. The manuscript was written by T.W.H., P.A.P., and J.M.F.

ACKNOWLEDGMENTS

This study was funded by the National Cancer Institute/NIH grants R01 CA131970 and R21 CA183627, and the Alzheimer's Drug Discovery Foundation grant ADDF no. 20101103. We thank Aditya Vaidya, Leo Serrebryanny, Irida Kastrati, Tiffany Sharma, and Jeanne Danes for experimental guidance. We thank Dr. Edward Seto for providing plasmids for the HDAC3 mutants

and the UIC DNA service facility for help with sequencing. We thank Dr. Greg Thatcher for thought-provoking discussion.

Received: March 6, 2017

Revised: June 10, 2017

Accepted: August 15, 2017

Published: September 21, 2017

REFERENCES

- Balasubramanian, S., Ramos, J., Luo, W., Sirisawad, M., Verner, E., and Buggy, J.J. (2008). A novel histone deacetylase 8 (HDAC8)-specific inhibitor PCI-34051 induces apoptosis in T-cell lymphomas. *Leukemia* 22, 1026–1034.
- Bardai, F.H., and D'Mello, S.R. (2011). Selective toxicity by HDAC3 in neurons: regulation by Akt and GSK3beta. *J. Neurosci.* 31, 1746–1751.
- Bhaskara, S., Knutson, S.K., Jiang, G., Chandrasekharan, M.B., Wilson, A.J., Zheng, S., Yenamandra, A., Locke, K., Yuan, J.L., Bonine-Summers, A.R., et al. (2010). Hdac3 is essential for the maintenance of chromatin structure and genome stability. *Cancer Cell* 18, 436–447.
- Bruzzese, F., Leone, A., Rocco, M., Carbone, C., Piro, G., Caraglia, M., Di Gennaro, E., and Budillon, A. (2011). HDAC inhibitor vorinostat enhances the antitumor effect of gefitinib in squamous cell carcinoma of head and neck by modulating ErbB receptor expression and reverting EMT. *J. Cell. Physiol.* 226, 2378–2390.
- Chakraborty, A.R., Robey, R.W., Luchenko, V.L., Zhan, Z.R., Piekarz, R.L., Gillet, J.P., Kossenkova, A.V., Wilkerson, J., Showe, L.C., Gottesman, M.M., et al. (2013). MAPK pathway activation leads to Bim loss and histone deacetylase inhibitor resistance: rationale to combine romidepsin with an MEK inhibitor. *Blood* 121, 4115–4125.
- Cossu-Rocca, P., Orru, S., Mironi, M.R., Sanges, F., Sotgiu, G., Ena, S., Pira, G., Murgia, L., Manca, A., Uras, M.G., et al. (2015). Analysis of PIK3CA mutations and activation pathways in triple negative breast cancer. *PLoS One* 10, e0141763.
- Ellis, M.J., Ding, L., Shen, D., Luo, J., Suman, V.J., Wallis, J.W., Van Tine, B.A., Hoog, J., Goiffon, R.J., Goldstein, T.C., et al. (2012). Whole-genome analysis informs breast cancer response to aromatase inhibition. *Nature* 486, 353–360.
- ENCODE Project Consortium (2012). An integrated encyclopedia of DNA elements in the human genome. *Nature* 489, 57–74.
- Fournel, M., Bonfils, C., Hou, Y., Yan, P.T., Trachy-Bourget, M.C., Kalita, A., Liu, J., Lu, A.H., Zhou, N.Z., Robert, M.F., et al. (2008). MGCD0103, a novel isotype-selective histone deacetylase inhibitor, has broad spectrum antitumor activity in vitro and in vivo. *Mol. Cancer Ther.* 7, 759–768.
- Frasor, J., Chang, E.C., Komm, B., Lin, C.Y., Vega, V.B., Liu, E.T., Miller, L.D., Smeds, J., Bergh, J., and Katzenellenbogen, B.S. (2006). Gene expression preferentially regulated by tamoxifen in breast cancer cells and correlations with clinical outcome. *Cancer Res.* 66, 7334–7340.
- Gao, Z., Chiao, P., Zhang, X., Lazar, M.A., Seto, E., Young, H.A., and Ye, J. (2005). Coactivators and corepressors of NF-kappaB in IkappaB alpha gene promoter. *J. Biol. Chem.* 280, 21091–21098.
- Garnett, M.J., Edelman, E.J., Heidorn, S.J., Greenman, C.D., Dastur, A., Lau, K.W., Greninger, P., Thompson, I.R., Luo, X., Soares, J., et al. (2012). Systematic identification of genomic markers of drug sensitivity in cancer cells. *Nature* 483, 570–575.
- Gharbi, S.I., Zvelebil, M.J., Shuttleworth, S.J., Hancox, T., Saghir, N., Timms, J.F., and Waterfield, M.D. (2007). Exploring the specificity of the PI3K family inhibitor LY294002. *Biochem. J.* 404, 15–21.
- Glozak, M.A., and Seto, E. (2007). Histone deacetylases and cancer. *Oncogene* 26, 5420–5432.
- Gray, G.K., McFarland, B.C., Rowse, A.L., Gibson, S.A., and Benveniste, E.N. (2014). Therapeutic CK2 inhibition attenuates diverse prosurvival signaling cascades and decreases cell viability in human breast cancer cells. *Oncotarget* 5, 6484–6496.
- Guenther, M.G., Lane, W.S., Fischle, W., Verdin, E., Lazar, M.A., and Shiekhhattar, R. (2000). A core SMRT corepressor complex containing

- HDAC3 and TBL1, a WD40-repeat protein linked to deafness. *Genes Dev.* 14, 1048–1057.
- He, B., Velaparthi, S., Pieffet, G., Pennington, C., Mahesh, A., Holzle, D.L., Brunsteiner, M., van Breemen, R., Blond, S.Y., and Petukhov, P.A. (2009). Binding ensemble profiling with photoaffinity labeling (BEPFL) approach: mapping the binding poses of HDAC8 inhibitors. *J. Med. Chem.* 52, 7003–7013.
- Heideman, M.R., Wilting, R.H., Yanover, E., Velds, A., De Jong, J., Kerkhoven, R.M., Jacobs, H., Wessels, L.F., and Dannenberg, J.H. (2013). Dosage-dependent tumor suppression by histone deacetylases 1 and 2 through regulation of c-Myc collaborating genes and p53 function. *Blood* 121, 2038–2050.
- Hsieh, C.L., Ma, H.P., Su, C.M., Chang, Y.J., Hung, W.Y., Ho, Y.S., Huang, W.J., and Lin, R.K. (2016). Alterations in histone deacetylase 8 lead to cell migration and poor prognosis in breast cancer. *Life Sci.* 151, 7–14.
- Insinga, A., Monestiroli, S., Ronzoni, S., Gelmetti, V., Marchesi, F., Viale, A., Altucci, L., Nervi, C., Minucci, S., and Pelicci, P.G. (2005). Inhibitors of histone deacetylases induce tumor-selective apoptosis through activation of the death receptor pathway. *Nat. Med.* 11, 71–76.
- Jonas, B.A., and Privalsky, M.L. (2004). SMRT and N-CoR corepressors are regulated by distinct kinase signaling pathways. *J. Biol. Chem.* 279, 54676–54686.
- Khan, N., Jeffers, M., Kumar, S., Hackett, C., Boldog, F., Khramtsov, N., Qian, X., Mills, E., Berghs, S.C., Carey, N., et al. (2008). Determination of the class and isoform selectivity of small-molecule histone deacetylase inhibitors. *Biochem. J.* 409, 581–589.
- Lai, C.J., Bao, R., Tao, X., Wang, J., Atayan, R., Qu, H., Wang, D.G., Yin, L., Samson, M., Forrester, J., et al. (2010). CUDC-101, a multitargeted inhibitor of histone deacetylase, epidermal growth factor receptor, and human epidermal growth factor receptor 2, exerts potent anticancer activity. *Cancer Res.* 70, 3647–3656.
- Lapierre, M., Linares, A., Dalvai, M., Duraffourd, C., Bonnet, S., Boulahtouf, A., Rodriguez, C., Jalaguier, S., Assou, S., Orsetti, B., et al. (2016). Histone deacetylase 9 regulates breast cancer cell proliferation and the response to histone deacetylase inhibitors. *Oncotarget* 7, 19693–19708.
- Li, Y., Jia, L., Ren, D., Liu, C., Gong, Y., Wang, N., Zhang, X., and Zhao, Y. (2014). Axl mediates tumor invasion and chemosensitivity through PI3K/Akt signaling pathway and is transcriptionally regulated by slug in breast carcinoma. *IUBMB Life* 66, 507–518.
- Liu, X.F., and Bagchi, M.K. (2004). Recruitment of distinct chromatin-modifying complexes by tamoxifen-complexed estrogen receptor at natural target gene promoters in vivo. *J. Biol. Chem.* 279, 15050–15058.
- Luu, T.H., Morgan, R.J., Leong, L., Lim, D., McNamara, M., Portnow, J., Frankel, P., Smith, D.D., Doroshow, J.H., Wong, C., et al. (2008). A phase II trial of vorinostat (suberoylanilide hydroxamic acid) in metastatic breast cancer: a California Cancer Consortium study. *Clin. Cancer Res.* 14, 7138–7142.
- Mahlknecht, U., Will, J., Varin, A., and Herbein, G. (2004). HDAC3, a class I histone deacetylase, interacts with the p38 pathway and suppresses MAPK11-Mediated ATF-2 activation and TNF gene expression. *Blood* 104, 599a.
- Mottamal, M., Zheng, S., Huang, T.L., and Wang, G. (2015). Histone deacetylase inhibitors in clinical studies as templates for new anticancer agents. *Molecules* 20, 3898–3941.
- Muller, B.M., Jana, L., Kasajima, A., Lehmann, A., Prinzler, J., Budczies, J., Winzer, K.J., Dietel, M., Weichert, W., and Denkert, C. (2013). Differential expression of histone deacetylases HDAC1, 2 and 3 in human breast cancer – overexpression of HDAC2 and HDAC3 is associated with clinicopathological indicators of disease progression. *BMC Cancer* 13, 215.
- Munster, P.N., Marchion, D., Thomas, S., Egorin, M., Minton, S., Springett, G., Lee, J.H., Simon, G., Chiappori, A., Sullivan, D., and Daud, A. (2009). Phase I trial of vorinostat and doxorubicin in solid tumours: histone deacetylase 2 expression as a predictive marker. *Br. J. Cancer* 101, 1044–1050.
- Neelapapu, R., Holzle, D.L., Velaparthi, S., Bai, H., Brunsteiner, M., Blond, S.Y., and Petukhov, P.A. (2011). Design, synthesis, docking, and biological evaluation of novel diazide-containing isoxazole- and pyrazole-based histone deacetylase probes. *J. Med. Chem.* 54, 4350–4364.
- Ontoria, J.M., Altamura, S., Di Marco, A., Ferrigno, F., Laufer, R., Muraglia, E., Palumbi, M.C., Rowley, M., Scarpelli, R., Schultz-Fademrecht, C., et al. (2009). Identification of novel, selective, and stable inhibitors of class II histone deacetylases. Validation studies of the inhibition of the enzymatic activity of HDAC4 by small molecules as a novel approach for cancer therapy. *J. Med. Chem.* 52, 6782–6789.
- Pflum, M.K., Tong, J.K., Lane, W.S., and Schreiber, S.L. (2001). Histone deacetylase 1 phosphorylation promotes enzymatic activity and complex formation. *J. Biol. Chem.* 276, 47733–47741.
- Pulukuri, S.M., Gorantla, B., and Rao, J.S. (2007). Inhibition of histone deacetylase activity promotes invasion of human cancer cells through activation of urokinase plasminogen activator. *J. Biol. Chem.* 282, 35594–35603.
- Rees, M.G., Seashore-Ludlow, B., Cheah, J.H., Adams, D.J., Price, E.V., Gill, S., Javadi, S., Coletti, M.E., Jones, V.L., Bodycombe, N.E., et al. (2016). Correlating chemical sensitivity and basal gene expression reveals mechanism of action. *Nat. Chem. Biol.* 12, 109–116.
- Richon, V.M., Sandhoff, T.W., Rifkind, R.A., and Marks, P.A. (2000). Histone deacetylase inhibitor selectively induces p21WAF1 expression and gene-associated histone acetylation. *Proc. Natl. Acad. Sci. USA* 97, 10014–10019.
- Ropero, S., Fraga, M.F., Ballestar, E., Hamelin, R., Yamamoto, H., Boix-Chornet, M., Caballero, R., Alaminos, M., Setien, F., Paz, M.F., et al. (2006). A truncating mutation of HDAC2 in human cancers confers resistance to histone deacetylase inhibition. *Nat. Genet.* 38, 566–569.
- Ruefli, A.A., Ausserlechner, M.J., Bernhard, D., Sutton, V.R., Tainton, K.M., Kofler, R., Smyth, M.J., and Johnstone, R.W. (2001). The histone deacetylase inhibitor and chemotherapeutic agent suberoylanilide hydroxamic acid (SAHA) induces a cell-death pathway characterized by cleavage of Bid and production of reactive oxygen species. *Proc. Natl. Acad. Sci. USA* 98, 10833–10838.
- Salisbury, C.M., and Cravatt, B.F. (2007). Activity-based probes for proteomic profiling of histone deacetylase complexes. *Proc. Natl. Acad. Sci. USA* 104, 1171–1176.
- Sandor, V., Senderowicz, A., Mertins, S., Sackett, D., Sausville, E., Blagosklonny, M.V., and Bates, S.E. (2000). P21-dependent G(1) arrest with downregulation of cyclin D1 and upregulation of cyclin E by the histone deacetylase inhibitor FR901228. *Br. J. Cancer* 83, 817–825.
- Singh, T.R., Shankar, S., and Srivastava, R.K. (2005). HDAC inhibitors enhance the apoptosis-inducing potential of TRAIL in breast carcinoma. *Oncogene* 24, 4609–4623.
- Tate, C.R., Rhodes, L.V., Segar, H.C., Driver, J.L., Pounder, F.N., Burow, M.E., and Collins-Burow, B.M. (2012). Targeting triple-negative breast cancer cells with the histone deacetylase inhibitor panobinostat. *Breast Cancer Res.* 14, R79.
- Taylor, B.S., Decarolis, P.L., Angeles, C.V., Brenet, F., Schultz, N., Antonescu, C.R., Scandura, J.M., Sander, C., Viale, A.J., Socci, N.D., and Singer, S. (2011). Frequent alterations and epigenetic silencing of differentiation pathway genes in structurally rearranged liposarcomas. *Cancer Discov.* 1, 587–597.
- Uehara, N., Kanematsu, S., Miki, H., Yoshizawa, K., and Tsubura, A. (2012). Requirement of p38 MAPK for a cell-death pathway triggered by vorinostat in MDA-MB-231 human breast cancer cells. *Cancer Lett.* 315, 112–121.
- Weiss, C., Schneider, S., Wagner, E.F., Zhang, X., Seto, E., and Bohmann, D. (2003). JNK phosphorylation relieves HDAC3-dependent suppression of the transcriptional activity of c-Jun. *EMBO J.* 22, 3686–3695.
- Xu, C., Soragni, E., Chou, C.J., Herman, D., Plasterer, H.L., Rusche, J.R., and Gottesfeld, J.M. (2009). Chemical probes identify a role for histone deacetylase 3 in Friedreich's ataxia gene silencing. *Chem. Biol.* 16, 980–989.

Zhang, Y., Ng, H.H., Erdjument-Bromage, H., Tempst, P., Bird, A., and Reinberg, D. (1999). Analysis of the NuRD subunits reveals a histone deacetylase core complex and a connection with DNA methylation. *Genes Dev.* **13**, 1924–1935.

Zhang, J., Kalkum, M., Chait, B.T., and Roeder, R.G. (2002). The N-CoR-HDAC3 nuclear receptor corepressor complex inhibits the JNK pathway through the integral subunit GPS2. *Mol. Cell* **9**, 611–623.

Zhang, X., Ozawa, Y., Lee, H., Wen, Y.D., Tan, T.H., Wadzinski, B.E., and Seto, E. (2005a). Histone deacetylase 3 (HDAC3) activity is regulated by interaction with protein serine/threonine phosphatase 4. *Genes Dev.* **19**, 827–839.

Zhang, Z., Yamashita, H., Toyama, T., Sugiura, H., Ando, Y., Mita, K., Hamaguchi, M., Hara, Y., Kobayashi, S., and Iwase, H. (2005b). Quantitation of HDAC1 mRNA expression in invasive carcinoma of the breast*. *Breast Cancer Res. Treat.* **94**, 11–16.

STAR★METHODS

KEY RESOURCES TABLE

REAGENT or RESOURCE	SOURCE	IDENTIFIER
Antibodies		
Rabbit polyclonal anti-HDAC1	Abcam	Ab7028 Lot GR225006-10; RRID:AB_305705
Rabbit polyclonal anti-HDAC2	Abcam	Ab124974 Lot GR97402-7; RRID:AB_11127303
Rabbit polyclonal anti-HDAC8	Abcam	Ab187139 Lot GR163583-5
Rabbit polyclonal anti-HDAC3	Abcam	Ab7030 Lot GR210866; RRID:AB_305708
Mouse Monoclonal anti-HDAC4	Santa Cruz	Sc-46672 Lot C2817; RRID:AB_627706
Mouse Monoclonal anti-HDAC5	Santa Cruz	Sc-133-225 Lot J2516; RRID:AB_2116791
Rabbit Monoclonal anti-HDAC6	Abcam	Ab117516 Lot GR164583-5; RRID:AB_10900382
Mouse Monoclonal anti-HDAC7	Santa Cruz	Sc-74563 Lot K1416; RRID:AB_2248191
Mouse Monoclonal anti-HDAC9	Santa Cruz	Sc-398003 Lot J2516
Mouse Monoclonal anti-HDAC10	Santa Cruz	sc-393417 Lot A2617
Mouse Monoclonal anti-HDAC11	Santa Cruz	Sc-390737 Lot B2417
Mouse Monoclonal anti-HDAC3	Santa Cruz	Sc376957 Lot K0916
Mouse monoclonal anti-HDAC3 clone 3G6	Millipore	05-813 Lot 2726719; RRID:AB_310021
Rabbit polyclonal anti-pHDAC3 (Ser424)	Cell Signaling	3815; RRID:AB_2264084
Rabbit Polyclonal anti-NCOR2	Abcam	Ab24551 Lot GR76751-1; RRID:AB_2149134
Rabbit Polyclonal anti-NCOR1	Abcam	Ab24552 Lot GR224645-1; RRID:AB_2149005
Rabbit polyclonal anti-pAKT	Cell Signaling	4060S Lot 16; RRID:AB_2315049
Mouse monoclonal anti-AKT	Cell Signaling	2967S Lot 17; RRID:AB_331160
Rabbit polyclonal anti-TBL1	Abcam	Ab24548 Lot GR252858; RRID:AB_2199904
Mouse monoclonal anti-pc-Jun (KM-1)	Santa Cruz	Sc-822 Lot L2116; RRID:AB_627262
Mouse monoclonal anti-c-Jun	Santa Cruz	Sc-74543 Lot C2417; RRID:AB_627262
Rabbit polyclonal anti-c-Jun	Protein Tech	10024-2-AP; RRID:AB_2129714
Rabbit monoclonal p-P65 (Ser536)	Cell Signaling	3033S Lot 14; RRID:AB_331284
P65	Cell Signaling	6956P Lot 1
Mouse monoclonal anti-pJNK	Cell Signaling	9255; RRID:AB_2307321
Rabbit polyclonal anti-JNK	Cell Signaling	9252; RRID:AB_2250373
Mouse monoclonal anti-pP38	Cell Signaling	92116; RRID:AB_331296
Rabbit monoclonal anti-P38	Cell Signaling	8690
Goat Anti-Mouse 680RD IRDye	LiCOR	926-68070; RRID:AB_10956588
Goat Anti-Mouse 800CW IRDye	LiCOR	925-32210; RRID:AB_2687825
Donkey Anti-Rabbit 800CW IRDye	LiCOR	925-32213
Anti-Rabbit IgG	Acam	Ab37415 Lot GR282404; RRID:AB_2631996
Bacterial and Virus Strains		
NEB 5-alpha Competent <i>E. coli</i>	New England Biolabs	C2987
Chemicals, Peptides, and Recombinant Proteins		
HDAC1	BPS Bioscience	50051 Lot 150528-A
HDAC2	BPS Bioscience	50002 Lot 130823-G
HDAC3	BPS Bioscience	50003 Lot 130819
HDAC8	Petukhov Laboratory, University of Illinois at Chicago	
CK2	New England Biolabs	P6010S Lot 0161608
Lambda Phosphatase	New England Biolabs	P0753S Lot 0131610
JNK1	ThermoFisher	PV3319 Lot 1722548B
Epidermal growth factor	R&D Systems	236-EG-01M
TNF-alpha	R&D Systems	210-TA

(Continued on next page)

Continued

REAGENT or RESOURCE	SOURCE	IDENTIFIER
IL-1 β	Sigma Aldrich	19401
IGF-1	Sigma Aldrich	18779
TGF- β 1	Sigma Aldrich	T7039
Photomate	This Paper	N/A
TCS JNK 6o	Tocris	3222
AR-A014418	Kozikowski Lab	
SB202190	Sigma Aldrich	S7067
LY294002	Selleckchem	S1105
IKK VII	Sigma Aldrich	401486
TBB	Sigma Aldrich	T0826
Photomate	This Paper	336447079
SAHA	Selleckchem	S1047
SP600125	Sigma Aldrich	S5567
Azide-PEG3-Biotin Conjugate	Sigma Aldrich	762024
Tris(2-carboxyethyl)phosphine hydrochloride (TCEP)	Sigma Aldrich	75259
CuSO ₄ (II)	ThermoFisher	BP346
Tris[(1-benzyl-1H-1,2,3-triazol-4-yl)methyl]amine (TBTA)	Sigma Aldrich	678937
Adenosine 5'-triphosphate disodium salt	Sigma Aldrich	FLAAS
IRDye 800CW Azide	LiCOR	929-60000
Protease inhibitor cocktail	Roche	4693159001
Phosphatase inhibitor mini tablets	ThermoFisher	88667
RPMI	ThermoFisher	11875-093
Improved MEM	Corning	10-024
MEM Non-Essential Amino Acids	ThermoFisher	11140-050
L-Glutamine	ThermoFisher	25030-081
Penicillin-streptomycin	ThermoFisher	15140-122
Glycerol	Invitrogen	15514-011
Tween-20	ThermoFisher	BP337
Igepal CA-630	Sigma Aldrich	I3021
HEPES	ThermoFisher	15630-080
Trypsin	ThermoFisher	15090-046
FBS	Sigma Aldrich	F0926
Bovine Serum Albumin	Sigma Aldrich	A2153
Glycerol	Invitrogen	15514-011
Fluor De Lys	Enzo Life Sciences	BML-KI104-005
N-Boc-Acetyl-L-Lysine 7-amido-4-methylcoumarin	Chem-Impex International, Inc.	11607
ON-TARGET plus Human siNCOR SMARpool	Dharmacon	L-003518-00-0005
ON-TARGET plus Non-Targeting siRNA	Dharmacon	D-001810-01
Lipofectamine 2000	Invitrogen	11268-019
Critical Commercial Assays		
Pierce BCA Protein Assay kit	ThermoFisher	23225
Deposited Data		
Photomate	Pubmed	336447079
Experimental Models: Cell Lines		
MCF-7	Dr. Debra Tonetti, University of Illinois at Chicago	
T47-D	Dr. Debra Tonetti, University of Illinois at Chicago	
ZR75-1	ATCC	CRL-1500

(Continued on next page)

Continued

REAGENT or RESOURCE	SOURCE	IDENTIFIER
MDA-MB-231	Dr. Claudia Osipo, Loyola University	
MDA-MB-468	Dr. Elizaveta Benevolenskaya, University of Illinois at Chicago	
MDA-MB-453	Dr. Angela Tyner, University of Illinois at Chicago	
BT-20	Dr. James Radosevich, University of Illinois at Chicago	
Recombinant DNA		
FLAG-HDAC3	Dr. Edward Seto, George Washington University	
FLAG-HDAC3 S405A	Dr. Edward Seto, George Washington University	
FLAG-HDAC3 S405A/S424A	Dr. Edward Seto, George Washington University	
Software and Algorithms		
GraphPad Prism	GraphPad Software Inc	http://www.graphpad.com/scientific-software/prism/
MatLab	MathWorks	https://www.mathworks.com/
Image Studio Lite	LiCor	https://www.licor.com/bio/products/software/image_studio_lite/
Other		
Odyssey Blocking Buffer	LiCOR	927-40000
Dynabeads M-280 Streptavidin	ThermoFisher	11206D
Dynabeads Protein A	ThermoFisher	10002D
Slide-A-lyzer Mini Dialysis Units	ThermoFisher	69550

CONTACT FOR REAGENT AND RESOURCE SHARING

Further information and requests for reagents may be directed to Dr. Pavel Petukhov (pap4@uic.edu)

EXPERIMENTAL MODEL AND SUBJECT DETAILS**Cellular Models**

Human cell lines MCF-7 and T47-D were obtained from Dr. Debra Tonetti (University of Illinois at Chicago) and were maintained in RPMI supplemented with 2 mM L-glutamine, 10% FBS, 1% non-essential amino acids, 1% antibiotics penicillin-streptomycin and 0.01 mg/ml human recombinant insulin at 37°C in 5% CO₂. The cell line ZR75-1 was obtained from ATCC and was maintained in RPMI supplemented with 2 mM L-glutamine, 1 mM sodium pyruvate, 10% FBS, 10 mM HEPES, 1% non-essential amino acids, and 1% antibiotics penicillin-streptomycin at 37°C in 5% CO₂. The breast cancer cell lines MDA-MB-231, MDA-MB-468, MDA-MB-453 and BT20, obtained from Dr. Clodia Osipo (Loyola University Chicago), Dr. Elizaveta Benevolenskaya (University of Illinois at Chicago), Dr. Angela Tyner (University of Illinois at Chicago) and Dr. James Radosevich (University of Illinois at Chicago) respectively, were routinely maintained in IMEM media (Corning) supplemented with 2mM L-glutamine, 10 mM HEPES, 10% FBS, 1% non-essential amino acids and 1% antibiotics penicillin-streptomycin at 37°C in 5% CO₂. Cell line authentication is routinely performed for MCF-7, T47D and MDA-MB-Cells using short tandem repeat (STR) methodology. All cell lines are routinely evaluated for mycoplasma contamination.

METHOD DETAILS**Fluorogenic Enzymatic Assays for Class I HDAC Isoforms**

Photomate IC₅₀ for class I recombinant HDACs was measured using previously published procedures (He et al., 2009; Neelapapu et al., 2011). All recombinant enzymes were purchased from BPS Bioscience. Photomate inhibits HDAC1, 2, 3 and 8 with LogIC₅₀ of -6.38 ± .08, -6.88 ± 0.06, -6.96 ± 0.06, and -5.64 ± 0.06, respectively. The data is reported as the average ± s. e. (n=3).

General Procedure for Photolabeling in Live Cells

For whole cell analysis: cells were plated in 6 cm dishes and grown to 90% confluence in 2 mL culture medium. The medium was replaced with 1 mL culture medium and pretreated with competitor (SAHA, 200 μM or DMSO control where applicable and then treated with 10 μM photomate or DMSO control. After 40 min at 37°C, the cells were cooled to 4°C and irradiated with 366 nm light (35 J/cm²). The medium was removed and the cells gently washed twice with PBS and then covered with 1 mL PBS. Cells were scraped from plate into Eppendorf tubes, spun down at 1,000 g for 5 minutes at 4°C, the supernatant removed and the cells resuspended in photolabeling lysis buffer (50 mM HEPES (pH 7.5), 150 mM NaCl, 0.7% Igepal, 5% glycerol, 1x protease inhibitor cocktail

(Roche) and 1x phosphatase inhibitor cocktail (ThermoFisher)). Samples were homogenized by vortexing, incubated on a rotating stand at 4°C for 1 hour, spun down at 20,000 g for 10 minutes at 4°C and the protein concentrations were determined by bicinchoninic acid assay (BCA). For gel based visualization, 35.2 µg of total lysate was incubated with 800CW azide conjugated IRDye at a concentration of 1.5x the probe, TCEP (0.25 mM), TBTA (0.1 mM), and CuSO₄ (0.50 mM) for 90 minutes at rt. Samples were then diluted with sample loading buffer, heated to 70°C for 10 minutes and separated by gel electrophoresis. Gels were transferred to nitrocellulose membranes with iBlot transfer system (P3 for 7 minutes) and visualized with Odyssey Sa imager. Membranes were then blocked with odyssey blocking buffer for 2 hours at 4°C, incubated with desired antibodies overnight at 4°C, washed 3x 5 minutes with PBST, incubated with relevant species of 680RD IRDye conjugated secondary antibody for 1 hour and simultaneously visualized at 700 and 800 nm with Odyssey Sa imager. Signals that 1) were competed by SAHA by at least 50% (quantified by densitometry) and 2) co-stained with a specific class I HDAC antibody were further analyzed.

For enrichment on streptavidin coated magnetic beads, 1 mg photomate labeled cell lysate was incubated with azide conjugated biotin according to 1.5x concentration of probe, TCEP (0.25 mM), TBTA (0.1 mM), and CuSO₄ (0.50 mM) for 90 minutes at rt. Samples were then left at -20°C overnight. Precipitated protein was spun down at 6,000 x g for 4 minutes at 4°C, and resuspended with brief sonication in 1 mL cold methanol. This was repeated twice and the pellets were resuspended in 1 mL 0.22% SDS in PBS by brief sonication and 10 minutes of heating at 60°C. Next, 20 µL of Dynabeads M-280 (ThermoFisher) were washed 2 x with 0.22% SDS in PBS, added into each reaction and incubated for 1.5 hours at rt. Beads were removed with a magnet and then washed 2 x with 0.22% SDS in PBS (500 µL), 2 x with modified PBS (500 mM NaCl) and 2 x with PBS.

For Western blot analysis, bound proteins were then suspended in LDS loading buffer and heated at 70°C for 10 minutes. Beads were removed with magnet and samples separated by gel electrophoresis at 100 volts. Gels were transferred to nitrocellulose membranes with iBlot transfer system (P3 for 7 minutes), blocked with odyssey blocking buffer for 2 hours at 4°C, incubated with desired antibodies at 4°C, washed 3x 5 minutes with PBST, incubated with relevant species of 680RD IRDye conjugated secondary antibody for 1 hour and visualized with Odyssey Sa imager.

For mass spectrometry based analysis, bound proteins were eluted in laemmli sample buffer, boiled for 10 minutes and eluant collected in a fresh Eppendorf tube. These samples were loaded onto a 15% gel and run into the gel approximately 1 inch at 20 volts (1 hour). One gel slab per lane was excised and gel pieces were destained in 50 mM NH₄HCO₃ in 50% ACN (v/v) until clear. Gel pieces were dehydrated with 100 µl of 100% ACN for 5 min, the liquid removed, and the gel pieces rehydrated in 10 mM DTT and incubated at 5°C for 60 min. Gel pieces were again dehydrated in 100% ACN, liquid was removed and gel pieces were rehydrated with 55 mM IAA. Samples were incubated at room temperature, in the dark for 45 min. Gel pieces were washed with 50 mM NH₄HCO₃ and dehydrated with 100% ACN. Gel pieces were rehydrated with 10 ng/µl trypsin, resuspended in 50 mM NH₄HCO₃ on ice for 1 h. Excess liquid was removed and gel pieces were digested with trypsin at 37°C overnight. Peptides were extracted with 50% ACN/5% FA, followed by 100% ACN. Peptides were dried to completion and resuspended in 2% ACN/0.1% FA. Peptides were cleaned with C18 ZipTips (Millipore) according to the manufacturer's instructions, followed by LC-MS/MS analysis.

Mass Spectrometry Analysis

The tryptic peptides were dissolved in 0.1% FA, directly loaded onto a reversed-phase pre-column (Acclaim PepMap 100, Thermo Scientific). Peptide separation was performed using a reversed-phase analytical column (Acclaim PepMap RSLC, Thermo Scientific). The gradient was comprised of an increase from 6% to 35% solvent B (0.1% FA in 98% ACN) over 12 min and climbing to 80% in 4 min then holding at 80% for the last 4min, all at a constant flow rate of 400 nL/min on an EASY-nLC 1000 UPLC system. The resulting peptides were analyzed by Q ExactiveTM hybrid quadrupole-Orbitrap mass spectrometer (ThermoFisher Scientific). The peptides were subjected to NSI source followed by tandem mass spectrometry (MS/MS) in Q ExactiveTM (Thermo) coupled online to the UPLC. Intact peptides were detected in the Orbitrap at a resolution of 70,000. Peptides were selected for MS/MS using NCE setting as 28; ion fragments were detected in the Orbitrap at a resolution of 17,500. A data-dependent procedure that alternated between one MS scan followed by 20 MS/MS scans was applied for the top 20 precursor ions above a threshold ion count of 1E4 in the MS survey scan with 15.0 s dynamic exclusion. The electrospray voltage applied was 2.0 kV. Automatic gain control (AGC) was used to prevent overfilling of the Orbitrap; 5E4 ions were accumulated for generation of MS/MS spectra. For MS scans, the m/z scan range was 350 to 1800. The resulting MS/MS data were processed using Mascot search engine (v.2.3.0). Tandem mass spectra were searched against Swissprot Homo Sapeins database. Trypsin/P was specified as cleavage enzyme allowing up to 2 missing cleavages. Mass error was set to 10 ppm for precursor ions and 0.02 Da for fragment ions. Carbamidomethyl on Cys were specified as fixed modification and oxidation on Met, acetylation on Protein N-term were specified as variable modifications. Peptide ion score was set > 20. Datasets collected from probe collected samples were compared to DMSO treated samples to remove non-specific interactions. Proteins that were not enriched in DMSO treated samples were then compared to probe plus SAHA treated samples and any protein in probe treated samples that was decreased by at least 50% is shown in [Table S1](#). This analysis was done using a custom Matlab script.

Serum Starvation Followed by Photolabeling

0.8x10⁶ or 0.5x10⁶ MCF-7 cells were plated in 6-well plates (corning) and grown in complete medium for 2 days. After 2 days the medium was replaced with either serum free medium (into the wells plated with 0.3x10⁶ cells or complete medium (into the wells plated with 0.15x10⁶ cells). The cells were incubated for an additional 48 hours followed by the "general procedure for photolabeling in live cells".

Treatment with Inhibitors, Cytokines and Growth Factors Followed by Photolabeling

0.3x10⁶ MDA-MB-231 cells were plated in 6-well plates and grown in complete medium for 2 days. Inhibitors of CK2 (TBB, 50 μ M), JNK (SP600125, 10 μ M or TCS 60 20 μ M), p38 (SB202190, 10 μ M) and IKK/NF- κ B (IKK-16, 10 μ M), Pi3K (LY294002, 20 μ M), GSK3 β (AR-A014418, 20 μ M) or cytokines/growth factors EGF, TNF- α , IGF-1 (all at 10 ng/mL) were added to the growth medium at the indicated concentrations and incubated for 2-12 hours. After incubation, the “general procedure for photolabeling in live cells” was carried out or cells were lysed without further treatment for analysis by Western blot.

Transfection of Mutant HDAC3 Followed by Photolabeling

2.1x10⁶ MDA-MB-231 cells were plated in 10 cm plates (Corning) and grown in complete medium for 2 days. After 2 days the medium was removed, the cells washed twice with PBS and medium containing 5% FBS without penicillin/streptomycin was added. 10 μ g of S405A, S424A, or Flag-HDAC3 plasmids were diluted with 500 μ L IMEM, and 500 μ L of IMEM containing Lipofectamine 2000 was added and the samples incubated at room temperature for 30 minutes. Plasmid-lipofectamine complexes were added to the 10 cm plates and cells were transfected for 24 hours. The following day, the medium was removed and the cells washed twice with PBS. Complete medium was added and the cells were incubated for 2 hours with complete medium followed by the “general procedure for photolabeling in live cells”.

Western Blotting

Protein samples were diluted with sample loading buffer containing DTT (Invitrogen), heated to 70°C for 10 minutes and separated by gel electrophoresis at 100 volts. Gels were transferred to nitrocellulose membranes with iBlot transfer system (P3 for 7 minutes) and visualized with Odyssey Sa imager. Membranes were then blocked with Odyssey blocking buffer for 2 hours at 4°C, incubated with desired antibodies overnight at 4°C, washed 3x5 minutes with PBST, incubated with relevant species of IRDye conjugated secondary antibody for 1 hour and visualized with Odyssey Sa imager. If additional antibody probing was necessary, membranes were stripped with 0.2 N NaOH for 30 minutes and the Western blotting procedure was repeated starting from blocking with Odyssey buffer.

Quantitation of Class I HDAC Isoforms in Breast Cancer Cell Lines

A standard curve of individual recombinant proteins ranging from 1-20 ng as well as 30 μ g cell lysate from MCF-7 cells were visualized by Western blotting procedure. Signal was quantified by densitometry, plotted and a linear regression fit using Graphpad Prism 6 software. Relative HDAC3 and phosphorylated HDAC3 abundance in the panel of breast cancer cell lines was quantified in a similar manner without use of a standard curve.

Photolabeling of Recombinant Proteins

Recombinant class I and II HDACs (500 ng) or standard dilutions ranging from .01 to 1.5 ng, in photolabeling lysis buffer were pretreated with competitor (SAHA 200 μ M) or DMSO control for 15 minutes when applicable and then treated with photomate (10 μ M) or DMSO control. After a 40-minute incubation, samples were cooled to 0°C and irradiated with 366 nm light (35 J/cm²). Samples were then incubated with azide conjugated 800CW IRDye at a concentration 1.5x the probe, TCEP (0.25 mM), TBTA (0.1 mM), and CuSO₄ (0.50 mM) for 90 minutes at rt. Samples were then diluted with loading buffer, heated to 70°C for 10 minutes and separated by gel electrophoresis at 100 volts. Gels were transferred to nitrocellulose membranes with iBlot transfer system (P3 for 7 minutes) and visualized with Odyssey Sa imager. Membranes were then blocked with Odyssey blocking buffer for 2 hours at 4°C, incubated with antibodies for class I HDACs overnight at 4°C, washed 3x5 minutes with PBST, incubated with anti-rabbit 680RD IRDye conjugated secondary antibody for 1 hour and visualized with Odyssey Sa imager.

Phosphorylation of Recombinant HDAC3

1 μ g recombinant HDAC3 was diluted with 20 μ L CK2 reaction buffer (New England Biolabs). 100 mM ATP was added, or vehicle for control reactions, followed by 200 U CK2 or 100 U JNK1. The reactions were incubated for 2 hours at 30°C. Samples were then dialyzed into photolabeling lysis buffer for use in “photolabeling of recombinant proteins”

Enzymatic Activity of HDAC3

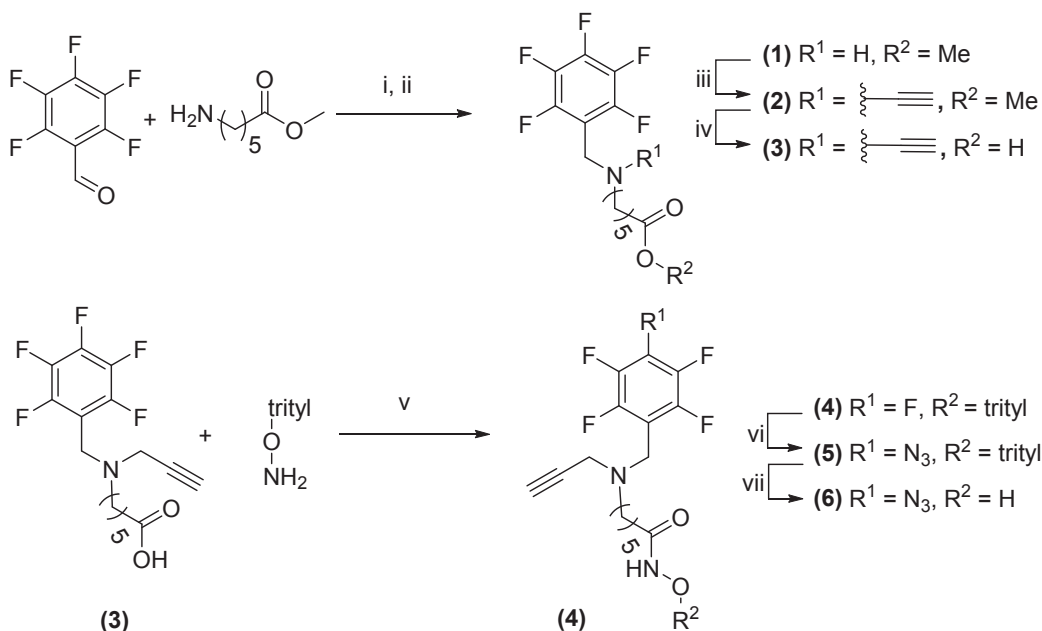
Serial dilutions of deacetylated *Fluor de Lys* substrate (0-40 μ M, Enzo Life Sciences) were prepared in KI-143 (25 mM Tris-HCl, pH 8.0, 137 mM NaCl, 2.7 mM KCl, and 1 mM MgCl₂). The amount of acetylated *fluor de lys* substrate that phosphorylated HDAC3 and HDAC3 could deacetylate in 30 minutes was compared to this curve. Recombinant proteins were diluted with KI-311 (25 mM Tris-HCl, pH 8.0, 137 mM NaCl, 2.7 mM KCl, and 1 mM MgCl₂, 1 mg/mL BSA) buffer to give 1 ng/ μ L stocks of each. 15 μ L of enzyme stock and 25 μ L of 5 mM substrate was added to a black half area 96 well plate (Corning) alongside 50 μ L of standard dilutions and incubated for 30 minutes rt. 50 μ L of 1 mg/mL trypsin and 5 μ M TSA in KI-143 buffer was added. The volume was made equal with KI-143 and the plate was read at excitation wavelength 360 nm and emission wavelength 460 nm using a Synergy 4 hybrid microplate reader from BioTek. Activity was determined using GraphPad Prism 6. Activity of 0.84 \pm .006 and 0.17 \pm .005 μ M substrate/hour were found for phosphorylated HDAC3 and non-phosphorylated HDAC3 respectively. The data is reported as the average \pm s. e. (n=3).

Immunoprecipitations

Six 10 cm plates were seeded with 0.8×10^6 MDA-MB-231 or MCF-7 cells and grown to 90% confluence. Cells were washed with PBS (2x 5 mL) followed by addition of 1 mL PBS. Cells were scraped from plate into Eppendorf tubes, spun down at 1000 rpm for 5 minutes at 4°C, the supernatant removed, and the cells resuspended in hypotonic buffer (10 mM Hepes (pH 7.5), 10 mM KCl, 0.05% (for MDA-MB-231 cells) or 0.4% (for MCF-7 cells) Igepal CA-630, 1x Protease inhibitor cocktail and 1x phosphatase inhibitor cocktail) until cell walls were compromised (verified by microscopic inspection). The mixture was spun down at 1,000 g for 5 minutes to provide the cytosol (supernatant) and nuclei (pellet). The nuclei were then homogenized in 200 μ L pull-down lysis buffer (20 mM Hepes (pH 7.5), 150 mM NaCl, 1.5 mM $MgCl_2$, 0.5% Igepal CA-630, 1x protease inhibitor cocktail and 1x phosphatase inhibitor cocktail) and incubated for 1 hour at 4°C on a rotating stand. Lysed nuclei were then centrifuged at 20,000 g for 10 minutes at 4°C to provide nuclear fraction (supernatant). Protein concentration was determined using Bradford assay and then diluted to 2 mg/mL with pull-down lysis buffer. 0.8 mg of lysate was incubated with 35 μ L protein A Dynabeads for 3 hours at rt and then stored for use at -20°C. For antibody bead conjugation, 60 μ L dynabeads (per reaction) were washed with PBS and separated into 2x 30 μ L aliquots. 15 μ g anti-HDAC3 (Abcam) antibodies or 15 μ g rabbit IgG control, each diluted with 150 μ L PBS, were added to either 30 μ L washed dynabead aliquot and incubated at rt for 2 hours. Bead antibody conjugates were then washed with 2x 1 mL PBS, 1 mL 0.2 N triethanolamine (pH 8.2) and incubated with 1 mL 25 mM dimethyl pimelidate in 0.2 N triethanolamine (pH 8.2) for 45 minutes at rt. After crosslinking bead-antibody conjugates were washed with 2x 1 mL 0.2 N triethanolamine (pH 8.2), resuspended in 0.1 N triethanolamine and incubated for 30 minutes at rt. Bead conjugates were then washed with 3x 1 mL PBS, 1 mL 0.2 N glycine (pH 2.6). Bead conjugates were then resuspended in 30 μ L PBS, added into 0.8 mg of a pre-cleared, 2 mg/mL nuclear extract described above, and incubated overnight at 4°C. The following day, beads were washed with 3x 1 mL pull-down lysis buffer and eluted with 3 x 50 mL 0.2 N glycine (pH 2.6). Eluates were pooled and 37.5 μ L TCA (100 w/v) solution was added followed by 15 μ L 1 M Tris (pH 8.5). Samples were incubated for 1.5 hours at 4°C and spun down at 20,000 g for 10 minutes at 4°C. The supernatant was removed and pellet was resuspended in 20 μ L Laemmli buffer. Samples were boiled for 5 minutes and electrophoretically separated. Proteins were transferred to nitrocellulose membranes with iBlot transfer system (P3 for 7 minutes), blocked with odyssey blocking buffer for 2 hours at 4°C, incubated with antibodies overnight at 4°C, washed 3x 5 minutes with PBST, incubated with anti-rabbit IRDye conjugated secondary antibody for 1 hour and visualized with Odyssey Sa imager.

Compound Synthesis

All chemicals were purchased from commercial sources (Aldrich, Matrix Scientific). All solvents were dried prior to use. Reactions were monitored by thin-layer chromatography (TLC) or by liquid chromatography (Waters, XSelect HSS CYANO 3.6 μ m mass spectrometry (LC/MS) (Shimadzu LCMS-2020). NMR spectra were obtained in deuterated chloroform or deuterated dimethylsulfoxide on a Bruker DPX-400 MHz spectrometer. NMR chemical shifts are reported in δ ppm downfield relative to TMS and J values are reported in Hz. High resolution mass spectrometry experiments (HRMS) were performed at the Mass spectrometry, Metabolomics and Proteomics Facility at University of Illinois at Chicago on a Thermo Finnigan LTQ FT ICR Hybrid Mass Spectrometer. Abbreviations DCM, dichloromethane, EtOAc, ethyl acetate, EDC, 1-ethyl-3-(3-dimethylaminopropyl)carbodiimide, HOBT, hydroxybenzotriazole, DMAP, 4-dimethylaminopyridine, DMF, dimethylformamide.



Methyl 6-(((perfluorophenyl)methyl)amino)hexanoate (1)

Pentafluorobenzaldehyde (10 mmol, 1.96 g) and amino methyl ester hydrochloride (10.6 mmol, 1.93 g) and Triethylamine (20 mmol, 2.02 g) was stirred in Methanol (40 mL) with molecular sieves under Nitrogen for 3 hours until imine formation was complete as monitored by TLC. After the imine had formed, the reaction was cooled to 0°C and NaBH₄ (16 mmol) was added portionwise over 20 minutes. The reaction was stirred for 24 hours, made basic by addition of 10% NaOH, and extracted with DCM (3x30mL). The DCM extract was dried over Na₂SO₄, and concentrated in vacuo. The crude product was purified by Silica chromatography eluting with gradient from 0–40% EtOAc in Hexanes to give compound 1 (2.6 g, 80%, colorless liquid).

¹H NMR (400 MHz, CDCl₃) δ 3.91 (s, 2H), 3.66 (s, 3H), 2.56 (t, J = 7.0 Hz, 2H), 2.30 (t, J = 7.4 Hz, 2H), 1.70 – 1.56 (m, 2H), 1.48 (m, 2H), 1.40 – 1.29 (m, 2H).

¹³C NMR (101 MHz, CDCl₃) δ 174.05, 51.47, 48.57, 40.50, 33.92, 29.54, 26.71, 24.74.

¹⁹F NMR (376 MHz, CDCl₃) δ -144.78 (dd, J = 22.8, 8.7 Hz, 2F), -156.24 (t, J = 20.7 Hz, 1F), -162.62 (td, J = 22.6, 8.8 Hz, 2F).

HRMS (ESI-TOF+) m/z calc'd for C₁₄H₁₆F₅NO₂ [M+H]⁺ : 326.1179, found: 326.1193

Methyl 6-(((perfluorophenyl)methyl)(prop-2-yn-1-yl)amino)hexanoate (2)

The secondary amine 1 (2.7 mmol, 0.88 g) was dissolved in acetonitrile (30 mL), K₂CO₃ (3.6 mmol, 0.5 g) and propargyl bromide (3mmol) was added, and the mixture was stirred for 12 hrs. The reaction volume was reduced in vacuo, diluted with water, and extracted with DCM (3x30 mL). The organic phase was concentrated and the crude product was purified with silica gel chromatography eluting with gradient 5–35% EtOAc in hexanes to give compound 2 (0.88 g, 90%, glassy solid).

¹H NMR (400 MHz, CDCl₃) δ 3.74 (s, 2H), 3.66 (s, 3H), 3.36 (s, 2H), 2.55 (t, J = 7.1 Hz, 2H), 2.29 (t, J = 7.5 Hz, 2H), 2.21 (t, J = 2.2 Hz, 1H), 1.66 – 1.54 (m, 2H), 1.49 (m, J = 14.5, 7.4 Hz, 2H), 1.32 (m, J = 15.0, 7.4 Hz, 2H).

¹³C NMR (101 MHz, CDCl₃) δ 174.07, 73.22, 52.65, 51.45, 44.88, 41.90, 33.98, 26.96, 26.63, 24.70.

¹⁹F NMR (376 MHz, CDCl₃) δ -142.06 (dd, J = 22.3, 8.1 Hz, 2F), -155.29 (t, J = 20.7 Hz, 2F), -162.41 (dt, J = 22.6, 8.0 Hz, 2F).

HRMS (ESI-TOF+) m/z calc'd for C₁₇H₁₈F₅NO₂ [M+H]⁺ : 364.1336, found: 364.1353

6-(((Perfluorophenyl)methyl)(prop-2-yn-1-yl)amino)hexanoic acid (3)

The tertiary amine 2 (2.4 mmol, 0.87 g) was dissolved in methanol:water (1:1, 30 mL) and NaOH (6 mmol, 0.24 g) was added. The reaction was stirred at room temperature under nitrogen for 3 hrs. Upon completion, as monitored by TLC, the reaction was brought to pH 4–5 with 10 % HCl and extracted with DCM (3x30 mL). The crude product was used in the next reaction without further purification (0.76 g, 90%, white solid).

¹H NMR (400 MHz, CDCl₃) δ 3.76 (s, 2H), 3.37 (s, 2H), 2.57 (t, J = 6.9 Hz, 2H), 2.33 (t, J = 7.3 Hz, 2H), 2.21 (s, 1H), 1.62 (m, 2H), 1.55 – 1.44 (m, 2H), 1.36 (m, 2H).

¹³C NMR (101 MHz, CDCl₃) δ 179.56, 73.53, 52.75, 44.97, 42.02, 34.06, 26.99, 26.71, 24.58.

¹⁹F NMR (376 MHz, CDCl₃) δ -141.91 (dd, J = 15.7, 6.8 Hz, 2F), -155.12 (t, J = 20.3 Hz, 1F), -162.34 (td, J = 21.3, 7.6 Hz, 2F).

HRMS (ESI-TOF+) m/z calc'd for C₁₆H₁₆F₅NO₂ [M+H]⁺ : 350.1179, found: 350.1196

6-(((Perfluorophenyl)methyl)(prop-2-yn-1-yl)amino)-N-(trityloxy)hexanamide (4)

To a mixture of intermediate 3 (2 mmol, 0.70 g), EDC (3 mmol, 0.47 g), HOBT (2.2 mmol, 0.34 g) and DMAP (2.2 mmol, 0.27 g) in CHCl₃ (30 mL) was added Et₃N (3 mmol) followed by immediate addition of o-tritylhydroxylamine (2.5 mmol, 0.68 g). The mixture was stirred at room temperature under nitrogen for 18 hrs. Upon completion, as monitored by TLC, the crude product was concentrated in vacuo, diluted with water, made acidic with 10 % HCl, washed with CHCl₃, neutralized with 10% NaOH (pH 7) and extracted with DCM (3x30 mL). The organic layers were collected and dried over Na₂SO₄. The crude product was then purified by silica chromatography eluting with a gradient of 5–35% EtOAc in hexanes to give compound 4 (75%, 0.91 g, white solid).

¹H NMR (400 MHz, DMSO) δ 10.13 (s, 1H), 7.32 (m, 15H), 3.69 (s, 2H), 3.28 (s, 3H), 3.14 (s, 1H), 2.37 (t, J = 6.9 Hz, 2H), 1.76 (t, J = 7.2 Hz, 2H), 1.26 (m, 2H), 1.16 (m, 2H), 0.94 (m, 3H).

¹³C NMR (101 MHz, DMSO) δ 170.65, 142.87, 129.35, 127.88, 127.77, 92.09, 78.60, 76.29, 52.56, 44.81, 41.57, 32.36, 26.75, 26.34, 24.98.

¹⁹F NMR (376 MHz, DMSO) δ -142.41 (dd, J = 24.3, 6.5 Hz, 2F), -156.15 (t, J = 22.1 Hz, 1F), -163.01 – -163.26 (m, 2F).

HRMS (ESI-TOF+) m/z calc'd for C₃₅H₃₁F₅N₂O₂ [M+H]⁺ 607.2384, found: 607.2439.

6-((4-Azido-2,3,5,6-tetrafluorobenzyl)(prop-2-yn-1-yl)amino)-N-(trityloxy)hexanamide (5)

NaN₃ (1.5 mmol, 0.91 g), Bu₄NN₃ (0.077 mmol, 0.02 g) and intermediate 4 (0.75 mmol, 0.45 g) were heated in DMF at 75°C for 18 hrs. The crude product was concentrated in vacuo, and then diluted with water. The water layer was extracted with DCM (3x30 mL) and the organic phases combined and concentrated to afford a brown solid. The solid was then passed through a short silica column eluting with 37.5% EtOAc in Hexanes to give compound 5 (0.19 g, 40%, colorless solid).

¹H NMR (400 MHz, DMSO) δ 10.14 (s, 1H), 7.32 (s, 15H), 3.67 (s, 2H), 3.28 (s, 2H), 3.15 (s, 1H), 2.37 (t, J = 6.9 Hz, 2H), 1.76 (t, J = 7.2 Hz, 2H), 1.25 (m, 2H), 1.16 (m, 2H), 0.94 (m, 2H).

¹³C NMR (101 MHz, DMSO) δ 170.71, 142.93, 129.41, 127.94, 127.83, 112.72, 92.15, 78.69, 76.34, 52.52, 45.01, 41.71, 32.42, 26.81, 26.40, 25.03.

¹⁹F NMR (376 MHz, C₆D₆) δ -143.32 (dd, J = 22.1, 9.5 Hz, 2F), -152.84 (dd, J = 22.4, 9.8 Hz, 2F).

HRMS (ESI-TOF+) m/z calc'd for C₃₅H₃₁F₄N₅O₂ [M+H]⁺ : 630.2488, found: 630.2545

6-((4-Azido-2,3,5,6-tetrafluorobenzyl)(prop-2-yn-1-yl)amino)-N-hydroxyhexanamide (6)

To a solution of Intermediate 5 (0.3 mmol, 0.19 g) in DCM was added MgBr₂ (3 mmol, 0.55 g). The reaction was stirred at room temperature under nitrogen for 15 minutes and then diluted with water and extracted with DCM (3x 30 mL). The pooled extracts were concentrated, dried over Na₂SO₄ and purified by silica chromatography eluting with a gradient of 0-10% MeOH in DCM to give compound 6 (80%, 0.09 g, colorless solid).

¹H NMR (400 MHz, DMSO) δ 10.30 (s, 1H), 8.63 (s, 1H), 3.69 (s, 2H), 3.35 – 3.27 (m, 2H), 3.13 (t, J = 2.1 Hz, 1H), 2.44 (t, J = 7.0 Hz, 2H), 1.91 (t, J = 7.3 Hz, 2H), 1.46 (m, 2H), 1.42 – 1.34 (m, 2H), 1.21 (m, 2H).

¹³C NMR (101 MHz, DMSO) δ 169.06, 112.27, 78.32, 75.95, 52.16, 44.61, 41.32, 32.27, 26.41, 26.24, 24.98.

¹⁹F NMR (376 MHz, DMSO) δ -143.32 (dd, J = 22.4, 9.8 Hz), -152.82 (dd, J = 22.7, 10.0 Hz).

HRMS (ESI-TOF+) m/z calc'd for C₁₆H₁₇F₄N₅O₂ [M+H]⁺ : 388.1388, found: 388.1418

QUANTIFICATION AND STATISTICAL ANALYSIS

Statistical analyses were performed with GraphPad Prism 6 software. All data are shown as mean ± s.e. Student's t-test (two-tailed) was used to measure statistically significant differences between groups. p value < 0.0005 was considered statistically significant for this study. One way Anova was used to determine statistically significant variance. p < .0001 was considered statistically significant.

DATA AND SOFTWARE AVAILABILITY

Datasets for photomate selectivity, and Matlab script for MS/MS protein ID are available upon request.